공학석사 학위논문

선형 시간-주파수 표현에서 모터와 기어박스의 고장 특성 감지를 위한 가중 잔차 레니 정보에 관한 연구

A Weighted Residual Rényi Information (WRRI) for Detecting Fault Feature of Motor and Gearbox in Linear Time-Frequency Representation

2020 년 8 월

서울대학교 대학원

기계공학부

윤 명 백

Abstract

A Weighted Residual Rényi Information (WRRI) for Detecting Fault Feature of Motor and Gearbox in Linear Time-Frequency Representation

Myeongbaek Youn
Department of Mechanical Engineering
The Graduate School
Seoul National University

Many studies have been conducted for fault detection of rotating machinery under varying speed conditions using time-frequency representation (TFR). However, the parameters of TFR have been selected by researchers empirically in most previous studies. Also, the previously proposed TFR measures do not suggest the optimal parameter for fault diagnosis. This paper thus proposed a TFR measure to select the parameter from the perspective of detecting fault features.

The proposed measure, Weighted Residual Rényi Information (WRRI), is based on Rényi Information, selected through a comparative study among previously suggested measures. WRRI, defined as a modified form of the input *atom* of Rényi Information, consists of two terms. The first term is the residual term that extracts the fault feature, and the second term is the weighting term that reduces the effect of noise.

The validation process consists of the two steps; 1) analytic signal, 2) motor, and gearbox signal. In the validation using an analytic signal, it confirmed that WRRI suggested a better parameter for detecting fault features than the Rényi Information. Also, in the validation using a motor testbed signal and gearbox testbed signal, it confirmed that WRRI was possible to select more suitable parameters for fault diagnosis than the Rényi Information.

Keyword : Time-frequency representation
Fault feature
Fault diagnosis
Rényi Information
Detectability
Motor
Gearbox

Student Number: 2018-28190

Table of Contents

Abstract ..... **i**

Table of Contents ..... **iii**

List of Tables ..... **iv**

List of Figures ..... **v**

Nomenclatures ..... **ix**

Chapter 1 . Introduction **1**

1.1 Introduction 1

Chapter 2 . TFR Measure for Readability **4**

2.1 Linear TFR 4

2.2 TFR Measures 11

2.3 Comparative Study of Previous Measure 13

Chapter 3 . TFR Measure for Detectability **16**

3.1 Fault Feature Detectability 16

3.2 Weighted Residual Rényi Information 22

Chapter 4 . Validation of the Proposed Measure **29**

4.1 Analytic Signals Having Fault Feature 29

4.2 Experiment Signal 33

Chapter 5 . Conclusion **57**

Bibliography **58**

국문 초록 **64**

List of Tables

Table 2-1. Comparative measure values for 3 topics 13

Table 4-1. Quantification result of triangular speed profile spectrogram of the gearbox 36

Table 4-2. Quantification result of sinusoidal speed profile spectrogram of the gearbox 36

Table 4-3. Quantification result of Scalogram of the gearbox depend on vanishing moment 40

Table 4-4. Quantification result of triangular speed profile spectrogram of the motor 45

Table 4-5. Quantification result of trapezoidal speed profile spectrogram of the motor 49

List of Figures

Figure 2-1. Target generalized Morse wavelets for different parameter sets (a) in time domain and (b) in frequency domain. For the time domain wavelet, the blue line is the real part of the wavelet, the orange line is the imaginary part, and the yellow line is the modulus.....8

Figure 2-2. Target wavelets for DWT up to 4 level, (a) kinds of wavelets having 4 vanishing moment except Haar wavelet, (b) Daubechies wavelets with different vanishing moments. For the time and frequency domain, the blue line is the first stage filter, the orange line is second stage filter, the yellow line is third stage filter to make a detail coefficient in DWT, and the purple line is forth stage filter to make an approximation coefficient in DWT.....10

Figure 2-3. Signal distribution for comparative study, (a) Trend, (b) Interference & Overlap, (c) Multi-component 13

Figure 3-1. Modeled raw signal having fault feature of (a) impulse signal, (b) characteristic frequency and spectrogram of (c) impulse signal, (d) characteristic frequency.....17

Figure 3-2. Mixture of two fault feature (a) raw signal, (b) spectral analysis, and (c) spectrogram 18

Figure 3-3. Rényi Information values depends on a window sample in STFT 18

Figure 3-4. Linear chirp with impulse type of fault feature (a) raw signal, (b) result of Rényi information, (c) spectrogram having minimum Rényi value, and (d) spectrogram for comparison..20

Figure 3-5. Partial plot of Figure 3-4 (c), (d) 20

Figure 3-6. Process of calculating WRRI.....23

Figure 3-7. Schematic illustration of the residual term 25

Figure 3-8. Schematic illustration of the residual term with noise component 25

Figure 3-9. Schematic illustration of the weighting term.....25

Figure 4-1. Analytic signals composed of (a) linear chirp only, (b)

linear chirp and impulse type of fault feature, (c) linear chirp and mixture of fault features, and (d) linear chirp and characteristic frequency.....30

Figure 4-2. (a) Index plot for WRRI and Rényi Information, (b) Spectrogram at 2.4% window size of total signal length, and (c) Spectrogram at 1.4% window size of total window length.....30

Figure 4-3. (a) Index plot for WRRI and Rényi Information, (b) Spectrogram at 2.2% window size of total signal length 31

Figure 4-4. (a) Index plot for WRRI and Rényi Information, (b) Spectrogram at 2.4% window size of total signal length, and (c) Spectrogram at 10% window size of total window length.....31

Figure 4-5. Triangular speed profile of (a) RPM, (b) health state signal, (c) fault state signal of the gearbox. Sinusoidal speed profile of (d) RPM, (e) health state signal, (f) fault state signal of the gearbox.....34

Figure 4-6. Triangular speed profile (a) measure value of the gearbox according to window size, (b) spectrogram at 0.56% window size, (c) spectrogram at 5% window size. 34

Figure 4-7. Sinusoidal speed profile (a) measure value of the gearbox according to window size, (b) spectrogram at 0.80% window size, (c) spectrogram at 5% window size. 36

Figure 4-8. Triangular speed profile measure value of the gearbox according to β and γ (a) Rényi Information, (b) WRRI, (c) Scalogram at $\beta = 1, \quad \gamma = 1$, (d) Scalogram at $\beta = 40, \quad \gamma = 4$.....38

Figure 4-9. Sinusoidal speed profile measure value of the gearbox according to β and γ (a) Rényi Information, (b) WRRI, (c) Scalogram at $\beta = 1, \quad \gamma = 1$, (d) Scalogram at $\beta = 40, \quad \gamma = 4$.....38

Figure 4-10. Measure value of the gearbox using MODWT (a) Triangular speed profile, (b) Sinusoidal speed profile. 39

Figure 4-11. Triangular speed profile (a) Index plot for WRRI and Rényi Information depend on the vanishing moment, (b) Scalogram using db8, (c) Spectrogram using db39.....39

Figure 4-12. Sinusoidal speed profile (a) Index plot for WRRI and

Rényi Information depend on the vanishing moment, (b) Scalogram using db10, (c) Spectrogram using db34.....40

Figure 4-13. Overall configuration of the PMSM testbed.....43

Figure 4-14. (a) Testbed target motor, (b) schematic cross-sectional view of PMSM, (c) inter-turn short in the PMSM 43

Figure 4-15. Triangular speed profile of (a) RPM, (b) health state signal, (c) fault state signal. Trapezoidal speed profile of (d) RPM, (e) health state signal, (f) fault state signal. 43

Figure 4-16. Triangular speed profile (a) Measure value comparison according to window size, (b) spectrogram at Rényi information measure minimum point, (c) spectrogram at WRRI measure minimum point 45

Figure 4-17. Resolution box example 45

Figure 4-18. VGGNet based CNN model for fault diagnosis with spectrogram as input.....47

Figure 4-19. Result of (a) Training loss, (b) Validation accuracy using 2.8% window size spectrogram, (c) Training loss, and (d) Validation accuracy using 10% window size spectrogram as an input.....47

Figure 4-20. Trapezoidal (a) Measure value comparison according to window size, (b) spectrogram at WRRI measure minimum point, (c) spectrogram at the 10% window size 49

Figure 4-21. Result of (a) Training loss, (b) Validation accuracy using 1.36% window size spectrogram, (c) Training loss, and (d) Validation accuracy using 10% window size spectrogram as an input.....50

Figure 4-22. Triangular speed profile measure value of the motor according to β and γ (a) Rényi Information, (b) WRRI, (c) Scalogram at $\beta = 1, \quad \gamma = 1$, (d) Scalogram at $\beta = 40, \quad \gamma = 4$.....52

Figure 4-23. Trapezoidal speed profile measure value of the motor according to β and γ (a) Rényi Information, (b) WRRI, (c) Scalogram at $\beta = 1, \quad \gamma = 1$, (d) Scalogram at $\beta = 40, \quad \gamma = 4$.....52

Figure 4-24. Measure value of the motor using MODWT (a) Triangular speed profile, (b) Trapezoidal speed profile.....53

Figure 4-25. Triangular speed profile of the motor (a) Index plot for WRRI and Rényi Information depend on the vanishing moment, (b) Scalogram using db4, (c) Spectrogram using db31.....54

Figure 4-26. Trapezoidal speed profile of the motor (a) Index plot for WRRI and Rényi Information depend on the vanishing moment, (b) Scalogram using db4, (c) Spectrogram using db22 54

Nomenclatures

$\|A\|_F$	Frobenius norm
C_i	Coefficient of sine function
$C_{X_n{}^2}, C_{W_n{}^2}, C_{X_nX_f}$	Correlation coefficient
$C_{X_nW_f}, C_{W_nX_f}, C_{W_nW_f}$	Correlation coefficient
$H(\omega)$	Heaviside unit step function
$K_{\beta,\gamma}$	Normalizing constant
L	Filter width
M_{JP}	Moment-type measure
M_s	Norm-type measure
$P_x\,(t,f)$	Time-frequency coefficient
$P_{\beta,\gamma}$	Wavelet duration
R_α	Rényi Information
R_{n_α}	Normalized Rényi Information
$\widetilde{V_{J,n}}$	Scale coefficient
$W(n,k)$	Noise component in Fourier domain
$W_f(n,k)$	Fault state noise component in Fourier domain
$W_n(n,k)$	Health state noise component in Fourier domain
$\widetilde{W_{J,n}}$	Wavelet coefficient
X	Fourier coefficient of the signal
$X_n(n,k)$	Health state component in Fourier domain
$X_f(n,k)$	Fault feature in Fourier domain
$e(n,k)$	Noise difference component in Fourier domain
i	Imaginary number
k	Positive integer
f	Frequency
f_0	Central frequency
f_1	Characteristic frequency
f_2	Characteristic frequency
f_3	Chirp increasing frequency
f_4	Chirp stating frequency
f_C	Frequency in sinusoidal component
f_{m}	Modulating related frequency
$\mathrm{f_x}$	TFR coefficients of fault state
$g_{l,j}$	Wavelet filter of DWT

$h_{l,j}$	Scaling filter of DWT
$\tilde{g}_{l,j}$	Wavelet filter of MODWT
$\tilde{h}_{l,j}$	Scaling filter of MODWT
$h(t)$	Window function
$h^*(t)$	Complex conjugate of a window function
j	Positive integer
l	Positive integer
m, n	Positive integer
$\mathrm{n_x}$	TFR coefficients of health state
s	Scale parameter
t	Time instant
u	Translation parameter
$w(t)$	Noise signal in time domain
x	Time domain signal
$x_n(t)$	Health state signal in time domain
$x_f(t)$	Fault component signal in time domain
$\Psi_{\beta,\gamma}(\omega)$	Generalized Morse wavelet
α	Positive integer
$\alpha_{3;\beta,\gamma}$	Demodulated skewness
β	Decay parameter
γ	Symmetry parameter
$\delta(t)$	Impulse signal
θ_c	Phase in each frequency component
π	Pi
τ	Integration variable
ψ	Mother wavelet
ψ^*	Complex conjugate of the mother wavelet

Chapter 1. Introduction

1.1 Introduction

As the facilities used in the industry become more complicated and the number of automation facilities increases, the demand for failure diagnosis has been increasing. To minimize downtime cost caused by equipment failure, interest in Condition Based Maintenance (CBM) has increased. Among the part of CBM, Prognostics and Health Management (PHM) technology collects status information, detects anomalies in the system, and predicts failure points in advance through analysis and predictive diagnosis [1]. In the case of the fault diagnosis algorithm developed in the PHM research field, dynamics of the system in the health and fault state are measured through sensors, and the algorithm is developed through spectral analysis mainly at a constant speed. The difference between the two states is expressed as a failure characteristic frequency or a harmonic form of the supply frequency [2]–[4]. However, in recent years, fault diagnosis for rotating equipment has been actively studied for diagnosis in a variable speed condition as well as a constant speed condition in consideration of applicability in a real industrial environment. Because the spectral analysis is no longer meaningful under variable speed conditions, PHM researchers tried to diagnose the target system using time-frequency representation (TFR). TFR is an expression method that can simultaneously check time and frequency information, and is frequently used because of the advantage of being able to identify frequency components that vary depending on time segments [5]. For this reason, researchers have used TFR mainly to extract fault features or develop an improved TFR suitable for fault diagnosis of each target system. For example, studies using TFR for extraction fault features, Hong and Liang [6] performed a study of extracting fault features based on wavelet decomposition from the rotating machinery. In the study, a fault feature separation

algorithm based on wavelet decomposition was proposed by calculating the contribution ratio using a Fourier transform for a multi-component signal. Park et al [7] used Wavelet transform to reduce the influence of the signal caused by variable speed. By using the wavelet transform to remove the effect of speed variation, the fault diagnosis of the planetary gearbox was performed through the residual term containing the fault feature. For studies that improved or applied TFR to suit each system, Peng, Peter, and Chu [8] proposed an improved Hilbert-Huang transform (HHT) for the diagnosis of rolling bearing failure and showed advantages in computing efficiency and time-frequency resolution compared to the existing wavelet transform (WT). Li and Liang [9] proposed a generalized synchrosqueezing transform as a modified form of the synchrosqueezing transform for diagnosing gearbox fault in variable speed. The proposed TFR improves time resolution by transposing the raw signal into an analytic signal, calculating the inverse synchrosqueezing wavelet transform (SWT)[10], and using additional instantaneous frequency. Feng, Chen, and Wang [11] successfully exploited the newly proposed ConceFT method for bearing fault diagnosis [12]. In applying the method, they designed a noise-tolerant diagnostic algorithm considering the modulation feature of the bearing vibration signal. Feng and Liang [13] exploited the adaptive optimal kernel (AOK) method, a signal-dependent kernel method, to diagnose wind turbine gearbox fault [14]. By applying the AOK method, the fault feature observed in a laboratory signal that in-situ the sun gear fault can be observed more clearly in the real wind turbine gearbox signal. In these studies, the type of TFR has been determined and the parameters are selected to develop the algorithm. However, the determined TFR's parameter was determined heuristically by the researchers. Even though the results of TFR varies largely depending on the TFR parameters, most studies do not consider this and chose TFR parameters heuristically. The results heuristically selected in previous studies showed sufficient performance in the study, but this TFR may not be the optimal result.

A step behind the fault diagnosis, researchers studying TFR in the field of signal processing suggested measures to select the TFR parameter from the energy concentration point of view for the target TFR. Jones and Parks [15] suggested a moment-based measure with the same form of kurtosis. In the same way as the characteristic of kurtosis, the peakedness of the target TFR is quantified. Stanković [16] suggest norm-based measure with the same form of L2 norm. Rényi [17] suggested a modified version of Shannon entropy, Rényi Information which still has the properties of entropy. And the normalized version of Rényi Information is proposed by considering the energy scale problem [18]. These measures were used to determine TFR parameters in terms of energy concentration or to design an optimal kernel [19]–[21]. However, the parameters selected using these measures do not guarantee the optimal parameter in terms of detecting the fault features. That is, the parameters are not the best representation for designing fault diagnosis algorithm. Focusing on this problem, this study focuses mainly on proposing measures in terms of detecting fault features. Firstly, we analyze and compare the existing measures. Secondly, we show that it does not propose the optimal parameters for detecting fault features. Then, we propose a measure that can select the optimal parameter from the viewpoint of detecting fault features. Verification of the proposed measure is first performed with analytically designed signals and the measure is verified through motor and gearbox experiment signals.

This paper is organized as follow, Chapter 2 reviewed previously proposed measures and analyzed their characteristics. Chapter 3 introduces the proposed measure, WRRI, based on the detecting fault feature perspective. In Chapter 4, the validation process proceeded with analytic signals, gearbox, and motor experiment signals. Finally, Chapter 5 described the conclusion of the paper and future work.

Chapter 2. TFR Measure for Readability

2.1 Linear TFR

The TFRs used in this study are Short Time Fourier Transform (STFT) and Wavelet Transform (WT) classified as Linear TFR [5]. STFT is calculated by combining the Fourier transform used in general spectral analysis and window function. Fourier transform takes the sinusoidal function as a basis and localizes the target signal segment in the frequency domain. Within the assumption that the signal segment is quasi-stationary, the STFT moves the window function and has a 3-d representation [22]. The mathematical formula of the STFT is as follows.

$$P_x(t,f) = \int x(\tau)h^*(\tau - t)e^{-2j\pi f\tau}\, d\tau \tag{2-1}$$

$$\int |h(t)|^2 dt = 1 \tag{2-2}$$

Where $h(t)$ is a window function, $h^*(t)$ is a complex conjugate of a window function. The window function has unit energy and mainly uses hamming or rectangular window function. The length of the window function is the most important parameter of the STFT in that it determines the time-frequency resolution that occurs due to the uncertainty principle of Heisenberg-Gabor [23]. If the window size is long, STFT makes the representation having good frequency resolution, and if the window size is short, it makes the representation having a good time resolution.

Unlike STFT, WT uses wavelets as a basis to decompose signals. Wavelet, which is a wavelike function, is defined as the reference form as a mother wavelet and the modified form using the scale parameter is defined as a child wavelet. WT performs correlation operation on the basis of these wavelets. The mathematical formula of the WT is as follows.

$$P_x\,(u,s) = \frac{1}{\sqrt{s}}\int x(t)\psi^*\left(\frac{t-u}{s}\right)dt \tag{2-3}$$

$$\int \psi(t)dt = 0 \tag{2-4}$$

Where u is a translation parameter, s is a scale parameter, ψ is mother wavelet, and ψ^* stands for the complex conjugate of the mother wavelet. For proper WT, the integration of the wavelet in the time domain should be satisfied zero. As the window function is moved in STFT, the wavelet is also moved in WT by changing the translation parameter. The scale parameter is a value corresponding to the frequency bin in the STFT and has a mathematical relationship with the central frequency of the mother wavelet in the frequency domain. The central frequency corresponding to each scale is calculated as $f = f_0/s$ where f_0 is the central frequency of the mother wavelet. The representation created by changing these parameters in WT becomes a multi-resolution TFR, so it has good time resolution in the high frequency domain and good frequency resolution in the low frequency domain.

A discrete version of the wavelet transform can be expressed by its formula by discretizing the parameters of CWT. The scale parameter and translation parameter are discretized as follows. Where m and n are integers.

$$s = s_0^m, u = ns_0^m u_0 \tag{2-5}$$

$$\psi_{m,n}(t) = s_0^{-m/2}\psi(s_0^{-m}t - nu_0) \tag{2-6}$$

$$P_x\,(m,n;\psi) = s_0^{-m/2}\int x(t)\psi^*(s_0^{-m}t - nu_0)dt \tag{2-7}$$

The DWT used in this study is the Maximum overlap DWT (MODWT). MODWT essentially performs the same calculations as DWT. However, unlike DWT, it provides highly redundant information and performs nonorthogonal transform. Since the number of 2^j samples is not necessary, the signal does not need to be extended, and multi-resolution analysis is still possible [24], [25]. When

DWT is expressed by the linear filtering process, MODWT operation is possible by not down-sampling at each filter level, and the mathematical relationship of the filter between DWT and MODWT is as follows [26].

$$\begin{cases} \tilde{g}_{l,j} = \dfrac{g_{j,l}}{\sqrt{2^j}} \\ \tilde{h}_{l,j} = \dfrac{h_{j,l}}{\sqrt{2^j}}, \end{cases} \qquad l = 1,2,3,\dots,L-1 \tag{2-8}$$

Where j is a positive integer, L is the filter width, $g_{l,j}, h_{l,j}$ are wavelet and scaling filters of DWT respectively. $\widetilde{g_{l,j}}$ and $\widetilde{h_{l,j}}$ mean wavelet and scaling filter of MODWT. The wavelet and scale coefficients of MODWT are $\widetilde{W_{j,n}}$, $\widetilde{V_{j,n}}$ respectively.

$$\begin{cases} \tilde{V}_{j,n} = \sum_{l=0}^{L_j-1} \tilde{g}_{l,j}\, X_{(n-l)\ mod\ N} \\ \widetilde{W}_{j,n} = \sum_{l=0}^{L_j-1} \tilde{h}_{l,j}\, X_{(n-l)\ mod\ N} \end{cases} \tag{2-9}$$

Where $L_j = (2^j - 1)(L-1) + 1$. At the stage of integer j, MODWT takes the transformation of the X as a form of vector $\widetilde{W_1}, \widetilde{W_2}, \dots, \widetilde{W_j}, \widetilde{V_j}$. The $\widetilde{W_j}$ and $\widetilde{V_j}$ has a dimension of N calculated as the product of $N \times N$ wavelet and scale coefficient.

For each TFR described above, I would like to explain the parameters to be compared using the measures to be introduced in this study. In the case of the STFT, the value of measure was examined by changing the window size. The overlap is also a user-configurable parameter, but the overlap is excluded from this study because the amount of information always increased by overlapping signals is a part to be set in relation to computational cost. In the case of WT, various types of wavelets were compared. For CWT, generalized Morse wavelets introduced by Daubechies and Paul [27] were used for comparison. The mathematical formula and

details of the generalized Morse wavelet were as follow.

$$\Psi_{\beta,\gamma}(\omega) = K_{\beta,\gamma} H(\omega) \omega^{\beta} e^{-\omega^{\gamma}} \tag{2-10}$$

$$P_{\beta,\gamma}{}^{2} = \frac{\omega_{\beta,\gamma}{}^{2} \Psi_{\beta,\gamma}{}''(\omega_{\beta,\gamma})}{\Psi_{\beta,\gamma}(\omega_{\beta,\gamma})} = \beta\gamma \tag{2-11}$$

$$\alpha_{3;\beta,\gamma} = i\frac{\gamma - 3}{P_{\beta,\gamma}} \tag{2-12}$$

Where $K_{\beta,\gamma}$ is normalizing constant, $H(\omega)$ is Heaviside unit step function, β is decay parameter, and γ is symmetry parameter. The parameter that characterizes the wavelet is $P_{\beta,\gamma}$ wavelet duration and $\alpha_{3;\beta,\gamma}$ demodulated skewness, which is a combination of decay and symmetry parameters [28], [29]. Like the figure that Jonathan drew in [29], but for other parameter combinations, Figure 2-1 for the parameter sets for comparison was drawn using a freely available MATLAB toolbox called JLAB.

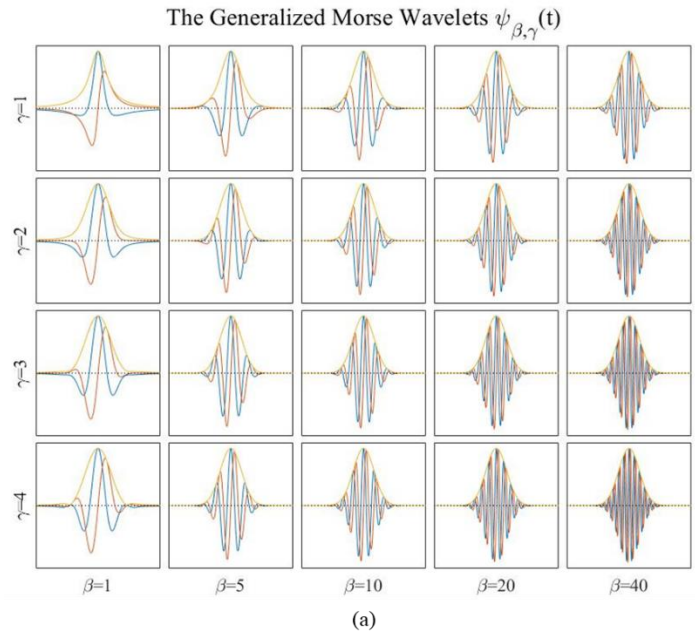

(a)

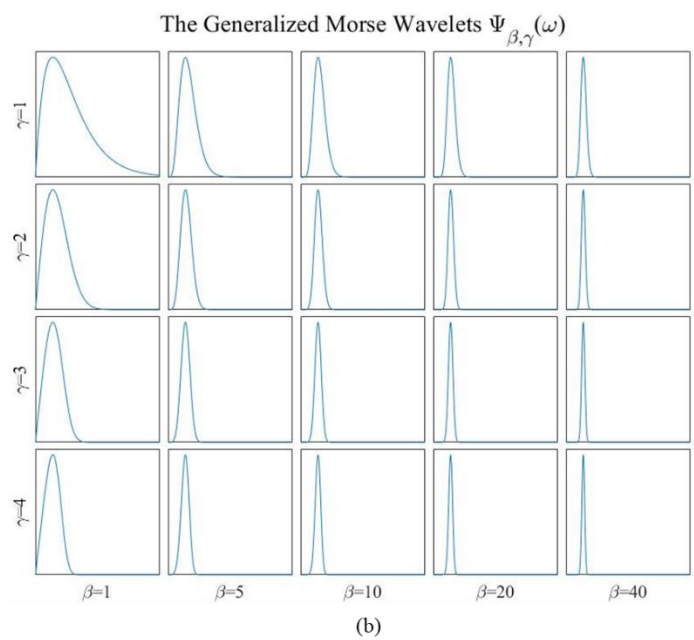

(b)

Figure 2-1. Target generalized Morse wavelets for different parameter sets (a) in time domain and (b) in frequency domain. For the time domain wavelet, the blue line is the real part of the wavelet, the orange line is the imaginary part, and the yellow line is the modulus.

In the figure (a) above, the x-axis was rescaled to the duration of each wavelet, and the y-axis was rescaled to the magnitude at t=0 of each wavelet. Also in figure (b), the x-axis was relocated to the central frequency of each wavelet. By changing the decay and symmetry parameters of the wavelet, we compared the wavelets of the Cauchy family ($\gamma = 1$), Gaussian family ($\gamma = 2$), Airy family ($\gamma = 3$), and Hyper-Gaussian family ($\gamma = 4$). For DWT, various types of wavelets are used for the comparative study of the previous and proposed measures. For example, Haar wavelets (haar), Symlet wavelet (sym), Coiflet wavelet (coif), Fejer-Korovkin wavelets (fk), and Daubechies wavelets. In the following description, the contents of the study were explained through changes according to the window size of the STFT. Afterward, in the validation process using testbed signals, the remaining TFRs and the parameters are used for validation through the difference in values for each measure.

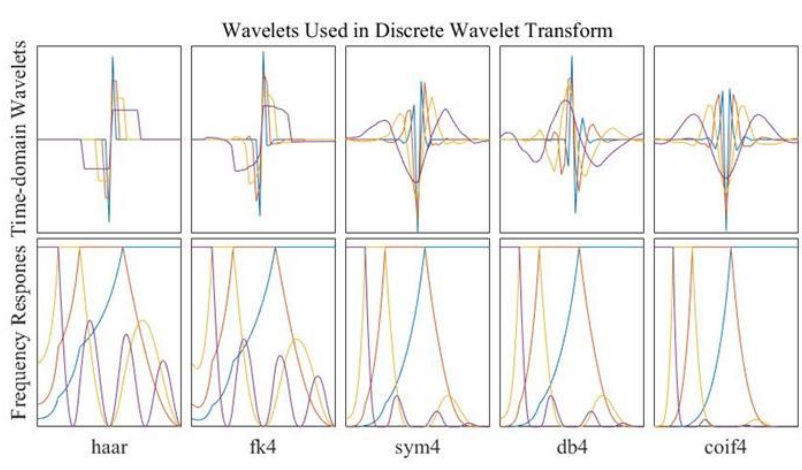

(a)

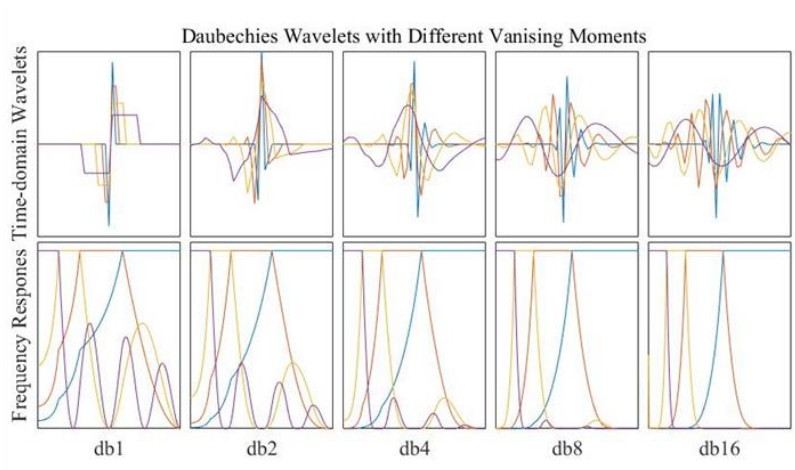

(b)

Figure 2-2. Target wavelets for DWT up to 4 level, (a) kinds of wavelets having 4 vanishing moment except Haar wavelet, (b) Daubechies wavelets with different vanishing moments. For the time and frequency domain, the blue line is the first stage filter, the orange line is second stage filter, the yellow line is third stage filter to make a detail coefficient in DWT, and the purple line is forth stage filter to make an approximation coefficient in DWT.

2.2 TFR Measures

In this chapter, we first analyze the TFR measures previously introduced. These measures were proposed for the purpose of turning TFR into an improved representation, which improves readability by making the representation clearer. For general use, the directionality of the measure worked to create a TFR that concentrates the energy of the signal [30]. Among the TFR measures studied so far, there are four representative measures to be analyzed in this paper. The first measure is the moment-type measure which is the same as Equation 2-13. This measure took a form of 4th order moment divided by 2nd order moment. To obtain high concentration and resolution, this measure is used to select the window size which is the parameter of Short Time Fourier Transform (STFT) [15]. Considering that the formula of measure is the same form of kurtosis, it can be inferred that this measure suggests a higher value as the peakedness of TFR increases. As a result, this measure has an ability to guide TFR to select parameters making more sharp representation.

$$M_{JP} = \frac{\sum_k \sum_n P_x^4\ (n,k)}{(\sum_k \sum_n P_x^2\ (n,k))^2} \tag{2-13}$$

The second measure is a norm-type measure which is the same as Equation 2-14. This measure took a form of L2 norm shape where the position of the coefficients is interchanged. This measure forms a simple formula with the characteristic that it does not discriminate against the low concentrated component. Additionally, this measure was also used in the STFT to select the optimal window size [16].

$$M_s = \left(\sum_{n=1}^{N} \sum_{k=1}^{N} |P_x\ (n,k)|^{1/2} \right)^2 \tag{2-14}$$

The third and fourth measure is an information-based measure derived from Shannon entropy. Shannon entropy is modified to be used in TFR as a Rényi

information to handle negative coefficient by the influence of interference term in certain TFR such as the Wigner-Ville distribution [17], [31]. Also, information-based measures have the characteristics of entropy, they play the same role as uncertainty measures of probabilistic distribution. In this case, the TFR is considered a multi-dimensional distribution, and the information measure quantifies the uncertainty of this representation. Therefore, this measure guides the parameters to create a more deterministic TFR, making it possible to make representation with high readability. The form of Rényi Information is the same as Equation 2-15, and hyper parameter α should be positive. But generally, the value of α is usually adopted as 3 because of its good properties[32]–[34]. In Baraniuk et al [34] study, detailed studies of its properties have been carried out, so the details are skipped in this paper. In Equation 2-16, it is a normalized version of Rényi Information. This measure was proposed to improve the limitations of Rényi Information with different values depending on the signal scale [18].

$$R_\alpha(P_x) = \frac{1}{1-\alpha}\log_2\left(\sum_k \sum_n P_x^\alpha\ (n,k)\right) \tag{2-15}$$

$$R_{n_\alpha}(P_x) = \frac{1}{1-\alpha}\log_2\left(\frac{\sum_k \sum_n P_x^\alpha\ (n,k)}{\sum_k \sum_n P_x\ (n,k)}\right)\ with\ \alpha \geq 2 \tag{2-16}$$

The measures introduced so far, the measures in Equation 2-13,14 quantify the peakedness of the representation, and the measures in Equation 2-15,16 quantify the uncertainty of the representation. This quantification makes it possible to select TFR with higher readability within a range of parameters. In the following chapter, a brief comparison of the four quantitative measures mentioned in this chapter was conducted and showed how measures work and what characteristics each one has. And based on the result of the measure comparative study, we adopt a one form from an existing measure to propose a new measure for detecting fault features.

2.3 Comparative Study of Previous Measure

By comparing the four representative measures introduced in the previous chapter, the characteristics of the TFR measure were illustrated. A comparative study is conducted with three topics that can appear in TFR. For the analysis of these topics, we use a 1-D distributed signal in a similar way to researcher Stankovi [16]. At this time, all 1-D distribution type signal L1 norm values are unified to 1 and the value was set differently only when checking the interference term. The first topic in Figure 2-3 (a) is about the trend of TFR measures. Target signal distribution is shown as (1) -(4) from uncertain to deterministic. The result of four representative measures can be seen in Table 2-1.

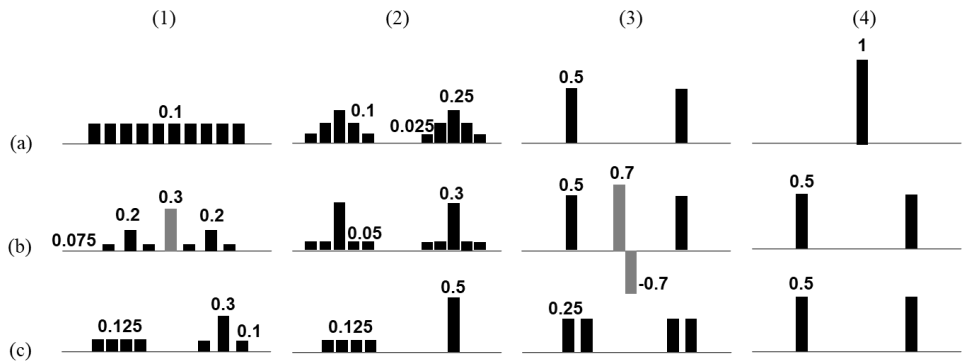

Figure 2-3. Signal distribution for comparative study, (a) Trend, (b) Interference & Overlap, (c) Multi-component

Table 2-1. Comparative measure values for 3 topics

Signal distribution	**Topic 1. Trend**				**Topic 2. Interference & Overlap**				**Topic 3. Multi-component**			
	(1)	**(2)**	**(3)**	**(4)**	**(1)**	**(2)**	**(3)**	**(4)**	**(1)**	**(2)**	**(3)**	**(4)**
L1 norm	1	1	1	1	1	1	2.4	1	1	1	1	1
M_{JP}	0.1	0.1675	0.5	1	0.1925	0.2	0.2569	0.5	0.1725	0.3125	0.25	0.5
M_s	10	8.3947	2	1	6.4394	8.3192	9.5329	2	6.7309	4.5	4	2
R	3.3219	2.4118	1	0	2.2420	2.0922	1	1	2.3818	1.4563	2	1
R_n	3.3219	2.4118	1	0	2.2420	2.0922	1.6315	1	2.3818	1.4563	2	1

As the signal distributions become shaper from (1) to (4), moment-type measure tends to increase as the signal distribution become shaper. The other measures tend to decrease as the signal distribution become shaper. This means that the measures show a monotonic tendency toward increasing or decreasing as the signals become more deterministic. Also, depending on the formula of the measure, the tendency may be increasing or decreasing.

The second topic in Figure 2-3 (b) is about interference and overlap signals. The (1), (2) expressed overlap term and, (3), (4) in (b) expressed interference term at TFR. For the overlap term. As for over term, it seems that norm-type measure is not suitable to choose sharp representation. Other measures could guide to having a sharp representation of this case. For the interference term, it can be seen that Rényi information ignores the impact of the interference term. This is a disadvantage for Rényi information that not possible to recognize interference term for Wigner-Ville distribution or modified version of Wigner-Ville distribution. Interestingly, the normalized Rényi information proposed to solve the scale problem shows good performance against interference terms.

The third topic in Figure 2-3 (c) is about multi-component. Through this topic, it can be seen the tendency of the measure about multi-component. This can be easily confirmed by comparing (2) and (3). The measures are said to be a sharper representation in (2) except for the norm-type measure. In other words, it can be seen that measures tend to focus on one large energy signal, and norm-type measures do not. Various interpretations are possible on this case, one is that the norm-based measure is effective in the TFR of rotating machinery having multi-components, and the other is that when the signal to noise ratio (SNR) is high, it is not effective because it guides in the direction of increasing noise component.

From the standpoint of developing a measure with the diagnosis of rotating machinery in the actual industrial site, normalized Rényi information can be regarded as the most appropriate measure. This is because normalized Rényi

information showed good performance for 2 of the 3 topics analyzed above, and confirmed that it tends to guide the TFR on the side that is more robust against noise for the last topic. Therefore, we propose a measure for detecting fault features based on normalized Rényi information in the next chapter.

Chapter 3. TFR Measure for Detectability

3.1 Fault Feature Detectability

Before suggesting a measure for the detecting fault feature, a description of the fault feature and how it is represented by the TFR measure are given in Chapter 3.1. A fault feature means a signal component that is not observed in a health state signal or is expressed differently from a health state signal. In the case of a fault state signal, the fault feature may be expressed as an independent component such as characteristic frequency, or it may appear as a modulation type accompany with a health state signal. In essence, the fault diagnosis is a quantification of the fault feature which is expressed as a difference between a health state and a fault state system. Therefore, in case of using TFR for a system on variable speed conditions, it is advantageous for the fault feature to be emphasized. This means that to diagnose a system, the parameter that best expresses the fault feature should be selected by a TFR measure. However, the existing measure has a limitation that it cannot guide to select the optimal parameters for detecting the fault feature.

To ascertain the issue more clearly, we confirm by modeling the fault feature that usually appears in rotating machinery. There are three types of fault feature signals modeled: the first is the impulse type of fault feature, the second is the characteristic frequency, and the last is a signal made from a mixture of the previous two fault features. The first modeling signal is the impulse train like Figure 3-1 (a) below. The impulse train signal expressed as a vertical line in a TF-plane. And it is the same as theoretical content when an impulse signal expressed on the Fourier domain [35]. Also, it can be seen that fine time resolution is to detect impulse type fault features well in case of STFT. Therefore, the measure for detecting fault feature should be able to guide the emphasis on time resolution. On the contrary, in the case of characteristic frequency, shown in Figure 3-1 (b). The characteristic frequency

expressed in the horizontal line in the spectrogram. For this type of fault feature, it is important to find the characteristic frequency clearly by improving the frequency resolution. To take a frequency resolution better, the TFR measure should guide the user to take the parameter having better frequency resolution.

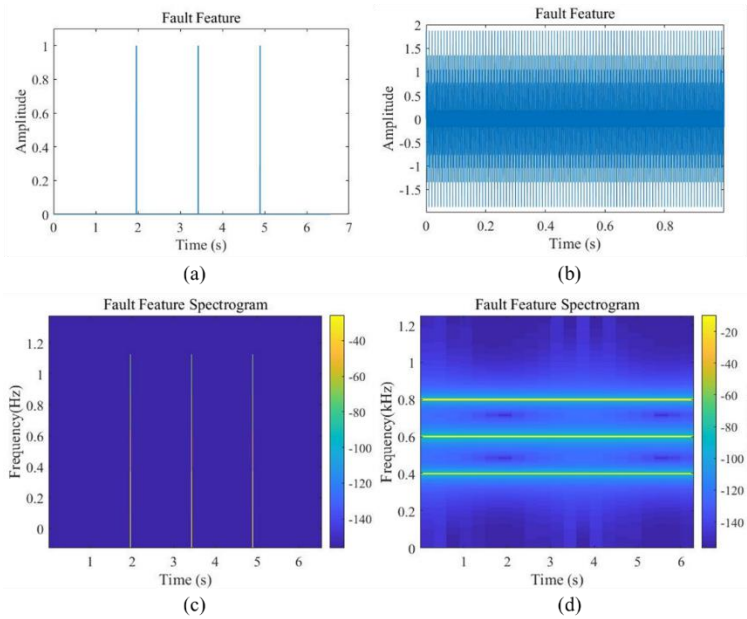

Figure 3-1. Modeled raw signal having fault feature of (a) impulse signal, (b) characteristic frequency and spectrogram of (c) impulse signal, (d) characteristic frequency

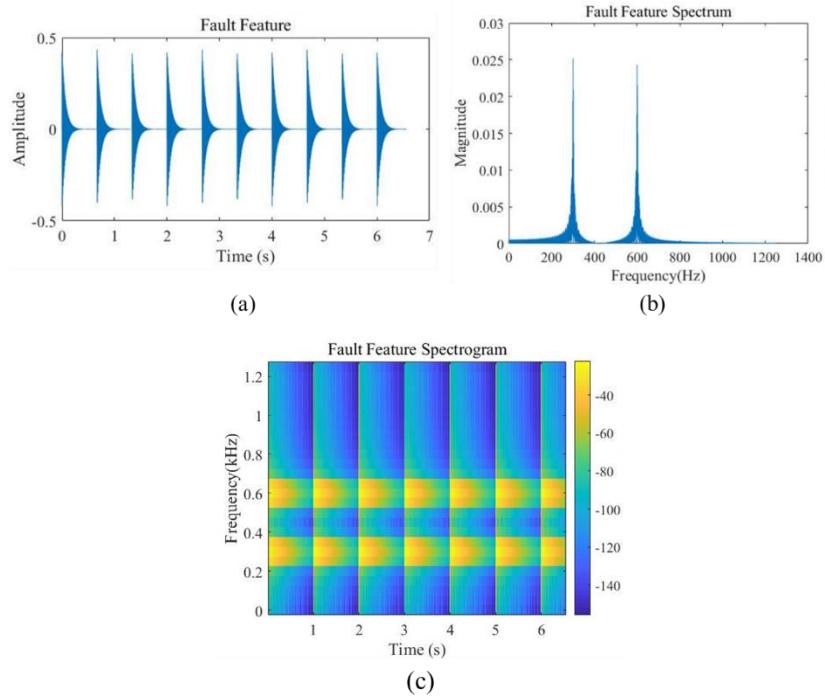

Figure 3-2. Mixture of two fault feature (a) raw signal, (b) spectral analysis, and (c) spectrogram

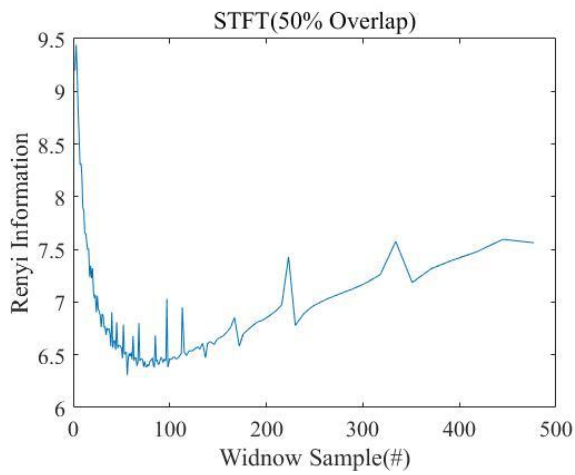

Figure 3-3. Rényi Information values depends on a window sample in STFT

The mixture of two fault feature was modeled by following the way of bearing signal similar with [36]. The modeled signal is given from the formula (3-1, 3-2).

$$x(t) = ke^{-\alpha t'}(\sin(2\pi f_1 t) + \sin(2\pi f_2 t)) \quad (3\text{-}1)$$

$$t' = mod(t, \frac{1}{f_0}) \quad (3\text{-}2)$$

where t is the time instant with a sampling frequency of 2500Hz for 6.5 seconds. $k = 0.25$ and $\alpha = 15$ is constant. $f_1 = 600\text{Hz}$ and $f_2 = 300\text{Hz}$ are characteristic frequency of the system. And $f_0 = 1.5\text{Hz}$ is a frequency related to modulating component, like bearing fault frequency (BPFO) in [36]. The function mod returns the value of modulus after division.

In the case of such a failure characteristic signal, it is difficult to expect an intuition about selecting an appropriate parameter. Therefore, in this case, the appropriate parameter should be selected using the TFR measure. For example, when using Rényi Information for the corresponding fault feature, it looks like Figure 3-3.

The above results indicate that the parameter to maximize the expression of the fault feature can be selected using the TFR measure. Going one step further, linear chirp with impulse type fault feature is modeled to see if these results were valid even when the driving frequency was present together. Hereinafter, a signal component which is the main trend such as a driving frequency is described as a ridge signal. The modeled signal was considered to have an effect that the amplitude increase as the frequency increases. And the effect of increasing the frequency of the impulse signal was considered.

$$x(t) = \left(4 + {}^{2}/_{3}\, t\right)\cos(2\pi f_3 t^2 + 2\pi f_4 t) + \delta(t) \quad (3\text{-}3)$$

where t is the time instant with a sampling frequency of 2500Hz for 6.5

seconds. $f_3 = 80\text{Hz}$ is a component related to the increase in the frequency of the linear chirp, and $f_4 = 100\text{Hz}$ is a value related to the start frequency. $\delta(t)$ is 10 impulse signals that appear at intervals that decrease linearly with increasing frequency.

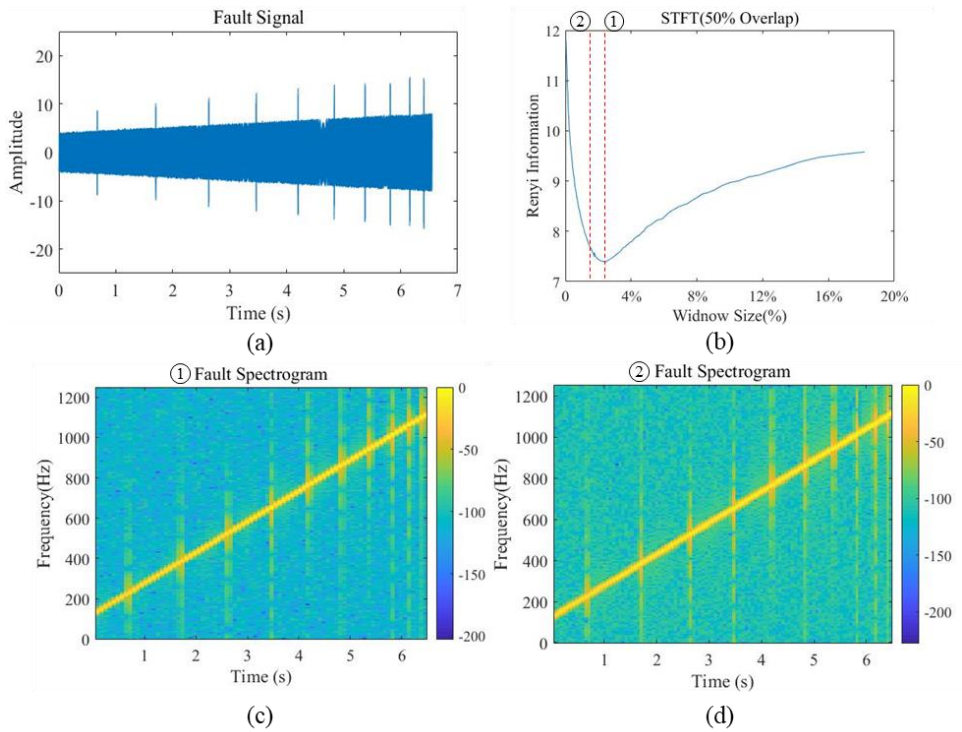

Figure 3-4. Linear chirp with impulse type of fault feature (a) raw signal, (b) result of Rényi information, (c) spectrogram having minimum Rényi value, and (d) spectrogram for comparison

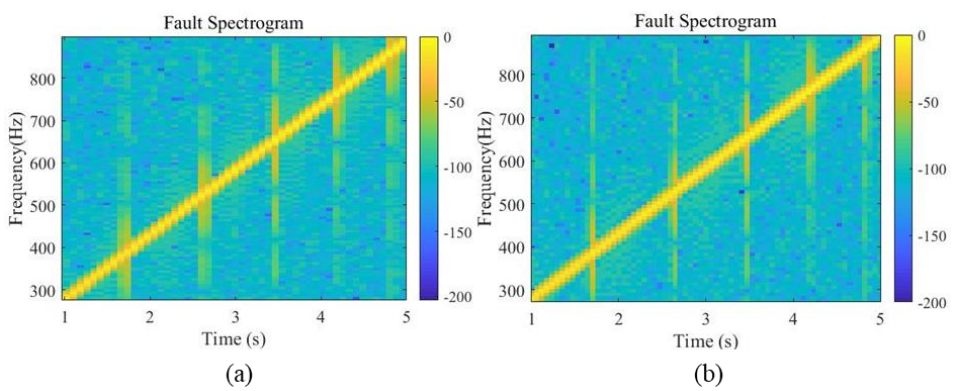

Figure 3-5. Partial plot of Figure 3-4 (c), (d)

Figure 3-4 (b) shows the result of using the existing measure, Rényi information, for a signal with a linear chirp and impulse type of fault feature added. That is, Rényi information guides us to select the window size that best represents this signal at the minimum point of the curve as a parameter. The window size corresponding to the minimum point is the size corresponding to 2.4% of the total signal length. For comparison, by drawing the spectrogram for the window size on the left slightly, Figure 3-4 (b) shows that the failure characteristics are better expressed while maintaining the tendency for the entire signal, not the plot of the window size indicated by Rényi information.

For a more detailed comparison, Figure 3-5 took a partial plot of Figure 3-4 (c), (d). Although the impulse type of fault feature is important in determining the window size that improves time resolution, Rényi Information does not seem to produce optimal results. It means that the window size guided by Rényi information can be a good measure for the concentration of the entire signal, but it cannot be used as an optimal measure to detect when fault features are mixed with the ridge signal. To overcome this limitation, we intend to propose a TFR measure that focuses on detecting fault features.

3.2 Weighted Residual Rényi Information

The core idea of the proposed measure for detecting fault features is to make use of the advantages of the existing Rényi information measure and to ensure that only the focus of the measure is detectability. At this time, since the object of detectability is a fault feature, a measure of a deformation type is proposed to emphasize this.

$$R_3(P_x) = -\frac{1}{2} log_2(\sum_k \sum_n P_x^3(n,k)) \tag{3-4}$$

$$P_x(n,k) = \sqrt{(F_x - N_x)}\sqrt{F_x} \tag{3-5}$$

$$F_x = \frac{\mathrm{f_x}}{\sum\sum \mathrm{n_x}}, \qquad N_x = \frac{\mathrm{n_x}}{\sum\sum \mathrm{n_x}} \tag{3-6}$$

where $P_x(n,k)$ is an *atom* that is an input of Rényi information as a variant of the TFR coefficient. $\mathrm{f_x}$ and $\mathrm{n_x}$ are TFR coefficients at the fault and health state respectively. F_x and N_x are TFR coefficients normalized by the total sum of the health state TFR coefficient. $R_3(P_x)$ is a Rényi information with basis alpha value 3. n and k are integer for the time and frequency axis. The process of calculating the proposed measure is shown in the figure below.

Firstly, TFR coefficients of health and fault state are normalized by using the total sum of the health state coefficient. According to the results of comparative studies of previously performed TFR measures, normalization was performed at the *atom* construction step to bring the advantage of normalized Rényi information. Next, the key idea of the proposed method is to change the shape of the *Atom*, $P_x(n,k)$ in equation (3-5). To explain the term, we introduce a simple mathematical derivation from the time domain to the time-frequency domain.

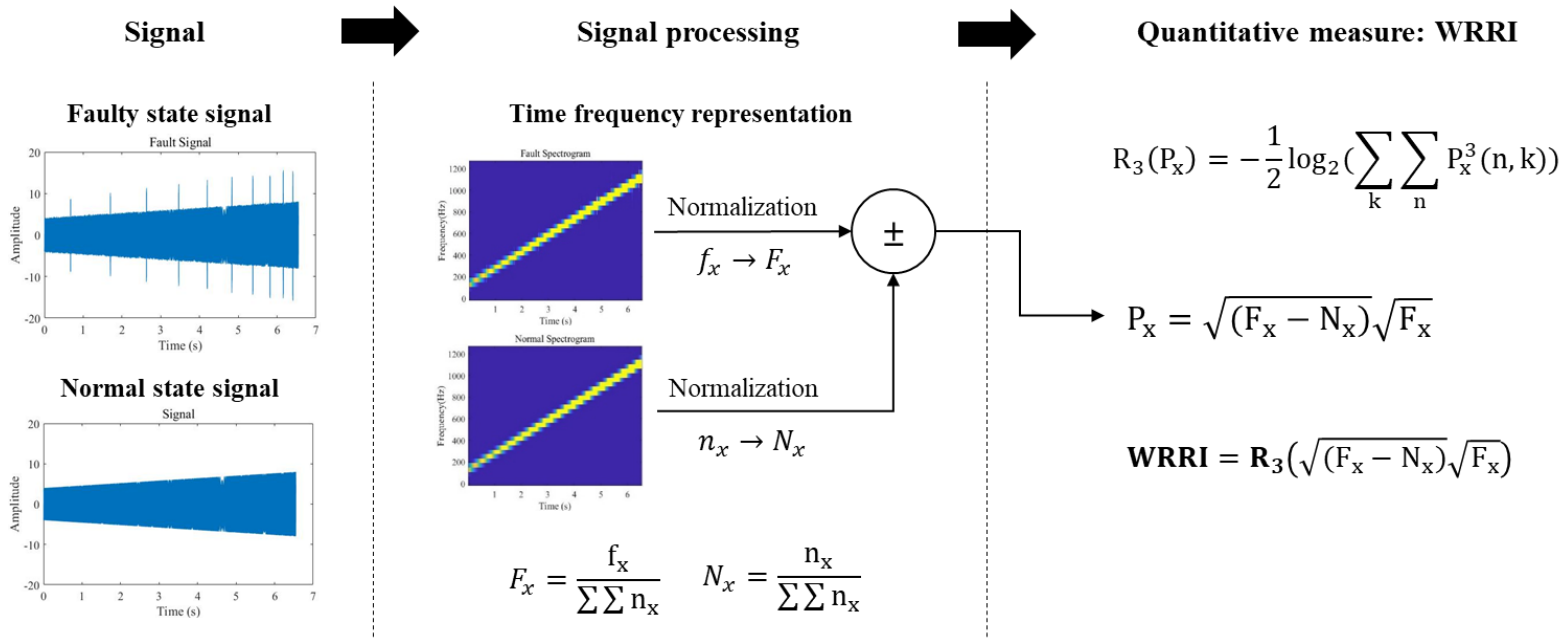

Figure 3-6. Process of calculating WRRI

When modeling a signal, it can be said that it consists of a signal with a noise term. In the case of a fault signal, the modeled signal can be expressed as the sum of the health, fault state signal, and noise signal. The health state signal can be expressed as a combination of sinusoidal functions, and the fault signal can be defined as a function that is affected by the health state signal and the fault characteristics of the system.

$$x(t) = x_n(t) + x_f(t) + w(t) \tag{3-7}$$

$$x_n(t) = \sum_{i=1}^{N} C_i \times \sin(2\pi \times f_C(i) \times t + \theta_c(i)) \tag{3-8}$$

$$x_f(t) = \boldsymbol{f}(x_n(t),\ Fault\ characteristic) \tag{3-9}$$

Interestingly, this expression is also available in the TF coefficient. TF coefficients of the fault signal can be represented by health state, fault state, and noise coefficients.

$$X(n,k) = X_n(n,k) + X_f(n,k) + W(n,k) \tag{3-10}$$

$$N_x = X_n(n,k) + W_n(n,k) \tag{3-11}$$

$$F_x = X_n(n,k) + X_f(n,k) + W_f(n,k) \tag{3-12}$$

The *atom*, $P_x(n,k)$, equation (3-5) based on the contents in equation (3-11, 3-12), the first term is the residual term same with equation (3-13). The residual term consists only of the TF coefficient and noise term. This component plays the role of extracting and highlighting the fault feature at the measure.

$$F_x - N_x = X_f(n,k) + e(n,k) \tag{3-13}$$

$$e(n,k) = W_f(n,k) - W_n(n,k) \tag{3-14}$$

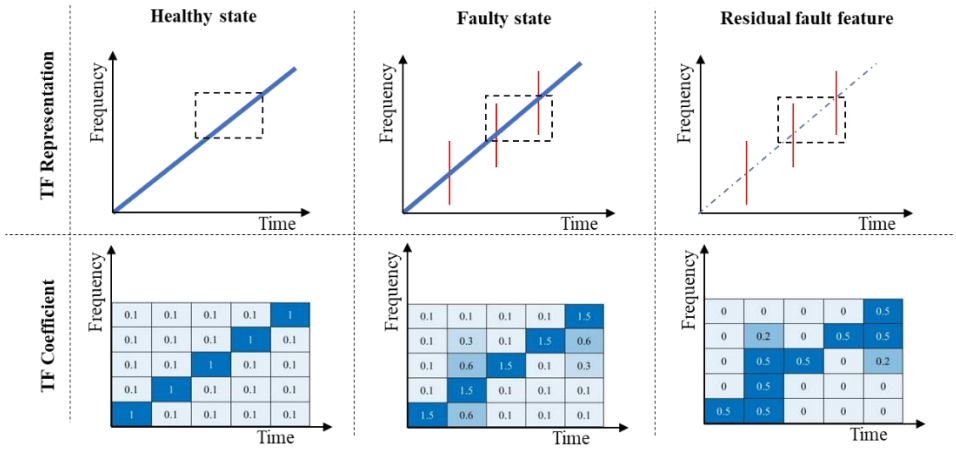

Figure 3-7. Schematic illustration of the residual term

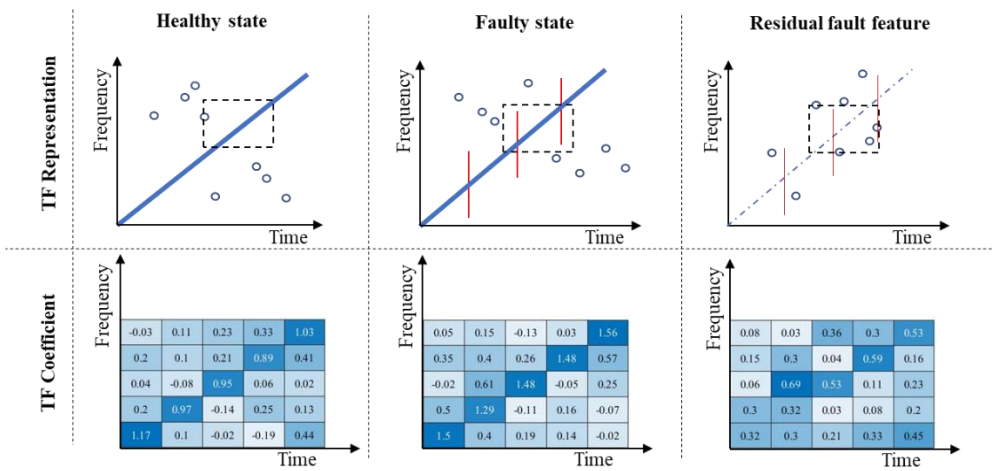

Figure 3-8. Schematic illustration of the residual term with noise component

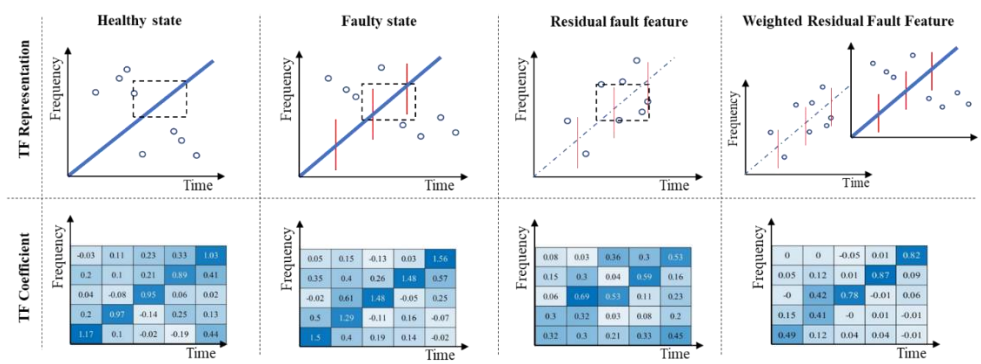

Figure 3-9. Schematic illustration of the weighting term

If the influence of the noise term among the components included in the residual term is very small or not, it will be emphasized in the fault feature as a schematic illustration in Figure 3-7. However, in most cases, signals contain noise component and their influence cannot be ignored.

As can be seen from the schematic Figure 3-8, it can be seen that it is difficult to extract the fault feature using the residual term due to the noise component. Therefore, it was necessary to emphasize the weight on the fault feature or reduce the influence on the noise component. The weighting term was designed for this purpose and simply took the simple form of multiplying the fault coefficient once more, resulting in the equation (3-5).

The purpose of the weighting term is to reduce the effect on the noise component by multiplying the fault coefficient to the residual term. The noise component remaining in the residual term is defined as the difference between the noise in the health and fault states as shown in equation (3-14), and this component is multiplied with the noise component in the fault coefficient. In general, noise components defined as white Gaussian have fluctuation values in TFR. It can be inferred that the effect of noise decreases because the weighting term creates a product form for different noise components. In order to examine the correlation of these components in more detail, a mathematical development of the proposed *atom* type and other forms was performed. First, for the existing measure, Rényi entropy, expressed by the TF coefficient defined by equations (3-11, 3-12). The TF coefficient of the fault signal expressed in the form of an *atom* is developed as shown in equation (3-15). At this time, for comparison with other *atom* types, the square form was used. Second, the residual term also could be expressed in the same way. It consists of fault feature component, health state noise component, and fault state noise component. The development equation is as shown in equation (3-16). Third, in the case of the *atom* composed of the product of the residual term and the fault coefficient, which is the proposed *atom*, it was also developed as in equation (3-17).

In the final form of expression from equation (3-15 – 17), there is a common square term consisting of a fault feature and fault state noise coefficients.

$$
\begin{aligned}
&P_x = F_x = \sqrt{F_x^2} \\
&F_x^2 = (X_n + X_f + W_f)^2 \\
&= {X_n}^2 + {X_f}^2 + {W_f}^2 + 2X_nX_f + 2X_fW_f + 2X_nW_f \\
&= (X_f + W_f)^2 + {X_n}^2 + 2X_nX_f + 2X_nW_f
\end{aligned} \tag{3-15}
$$

$$
\begin{aligned}
&P_x = \sqrt{(F_x - N_x)(F_x - N_x)} \\
&(F_x - N_x)^2 = (X_f + W_f - W_n)^2 \\
&= {X_f}^2 + {W_f}^2 + {W_n}^2 + 2X_fW_f - 2W_nX_f - 2W_nW_f \\
&= (X_f + W_f)^2 + {W_n}^2 - 2W_nX_f - 2W_nW_f
\end{aligned} \tag{3-16}
$$

$$
\begin{aligned}
&P_x = \sqrt{(F_x - N_x)F_x} \\
&(F_x - N_x)F_x = (X_n + W_f - W_n)(X_f + W_f) \\
&= {X_f}^2 + {W_f}^2 + 2X_fW_f - W_nX_f - W_nW_f \\
&= (X_f + W_f)^2 - W_nX_f - W_nW_f
\end{aligned} \tag{3-17}
$$

$$1 = C_{{X_n}^2} = C_{{W_n}^2} \tag{3-18}$$

$$1 > C_{X_nX_f} \gg C_{X_nW_f}, C_{W_nX_f}, C_{W_nW_f} \tag{3-19}$$

The other components of the development equation have a correlation within the components as summarized in equations (3-18, 3-19). Regarding the correlation between the ridge signal, the fault feature, and the noise term, it is based on the fact that the fault feature is dependent on the ridge signal and the noise components are independent of each other. In summary, based on the composition of expression and their correlation within the components, the dominant trend of WRRI consists only of square terms consisting of fault features and fault state signals. However, the other form of an *atom* cannot ignore the impact on other components. For example, in the case of Rényi Information, it can be expected that the measure will focus on the ridge signal because not only does ${X_n}^2$ term exist, but the other components cannot also ignore its impact. In the form of the *atom* that uses only residual, there are also

components that cannot be ignored, such as W_n^2 term. Since the term refers to noise acquired under the health state, the *atom* having residual form means that it is vulnerable to the noise component. Therefore, we showed that the proposed *atom*, consisting of the product of the weighting term and residual term, has an appropriate form to detect the fault feature. In addition, by using this *atom* in the Rényi information, it retained its good properties.

In the next chapter, we check the validity of our proposed measure, WRRI and the existing measure, Rényi Information, based on the fault signals

Chapter 4. Validation of the Proposed Measure

The validation process was conducted using two groups of signals. One is analytic signals that have a linear chirp as a ridge signal and have each of three fault features; impulse type of fault feature, characteristic frequency, a mixture of two fault features. The other is experiment signals consisting of signals obtained from the motor testbed and signals obtained from the gearbox testbed. As a target TFR for comparing WRRI and Rényi information, the comparative study results for each parameter of STFT, CWT, and DWT were described.

4.1 Analytic Signals Having Fault Feature

The analytic signal is composed of the sum of ridge signal and fault feature, and for convenience, it is assumed that the two are independent components. Ridge signal used linear chirp signal, and fault feature used the three fault features used in the previous Chapter 3. The linear chirp signal is designed to increase the amplitude linearly at the high rotational frequency by partially reflecting the characteristics of the rotating machinery. The modeling formula of linear chirp and modeled fault signals are as follows.

$$x(t) = \left(4 + {}^{2}/_{3}\, t\right) \cos 2\pi(100t + 80t^2) \qquad (4\text{-}1)$$

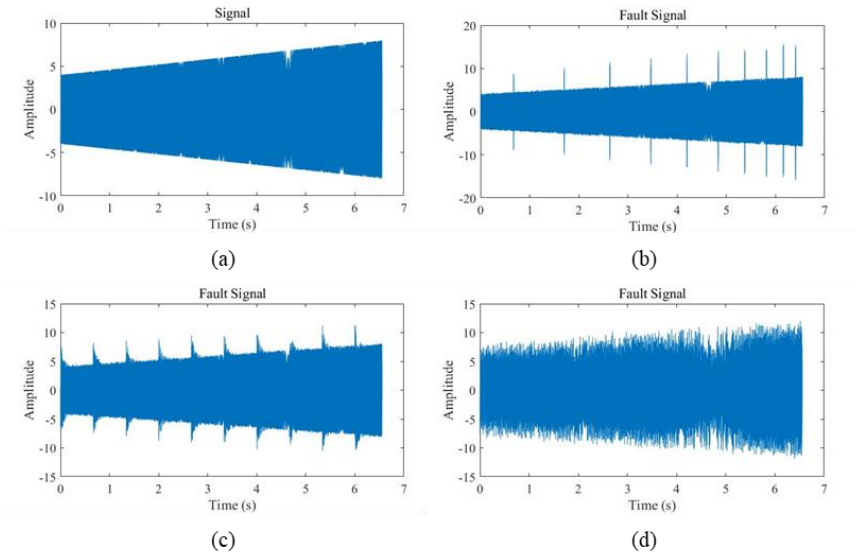

Figure 4-1. Analytic signals composed of (a) linear chirp only, (b) linear chirp and impulse type of fault feature, (c) linear chirp and mixture of fault features, and (d) linear chirp and characteristic frequency

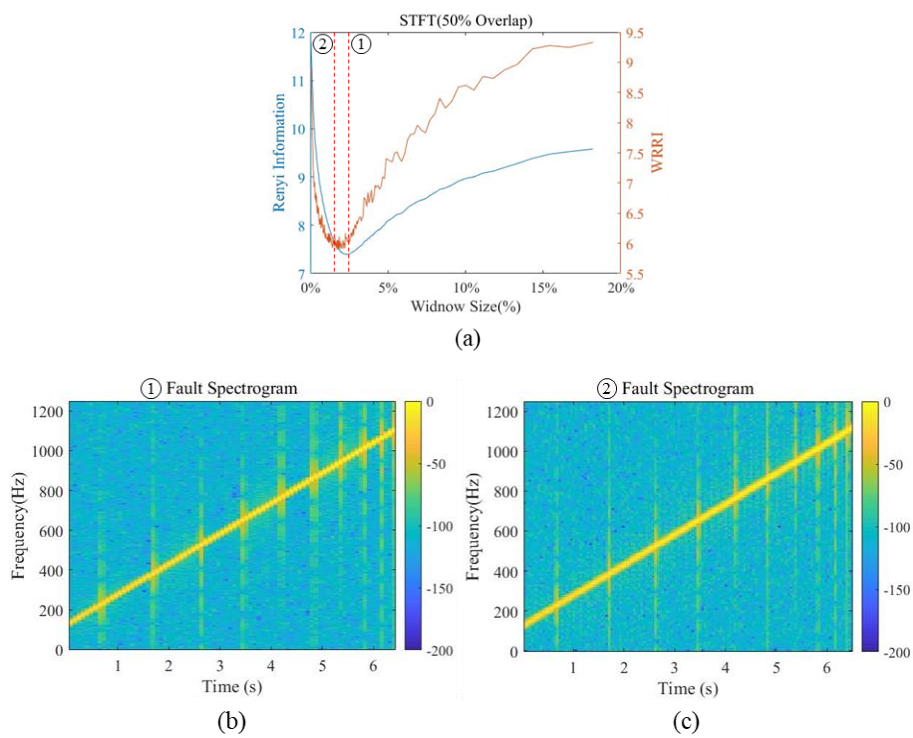

Figure 4-2. (a) Index plot for WRRI and Rényi Information, (b) Spectrogram at 2.4% window size of total signal length, and (c) Spectrogram at 1.4% window size of total window length

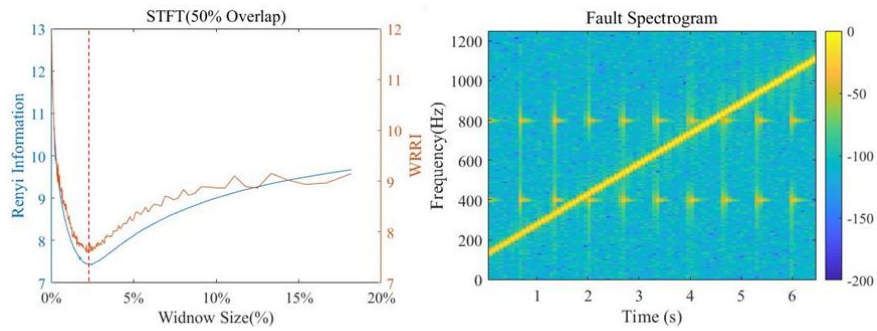

Figure 4-3. (a) Index plot for WRRI and Rényi Information, (b) Spectrogram at 2.2% window size of total signal length

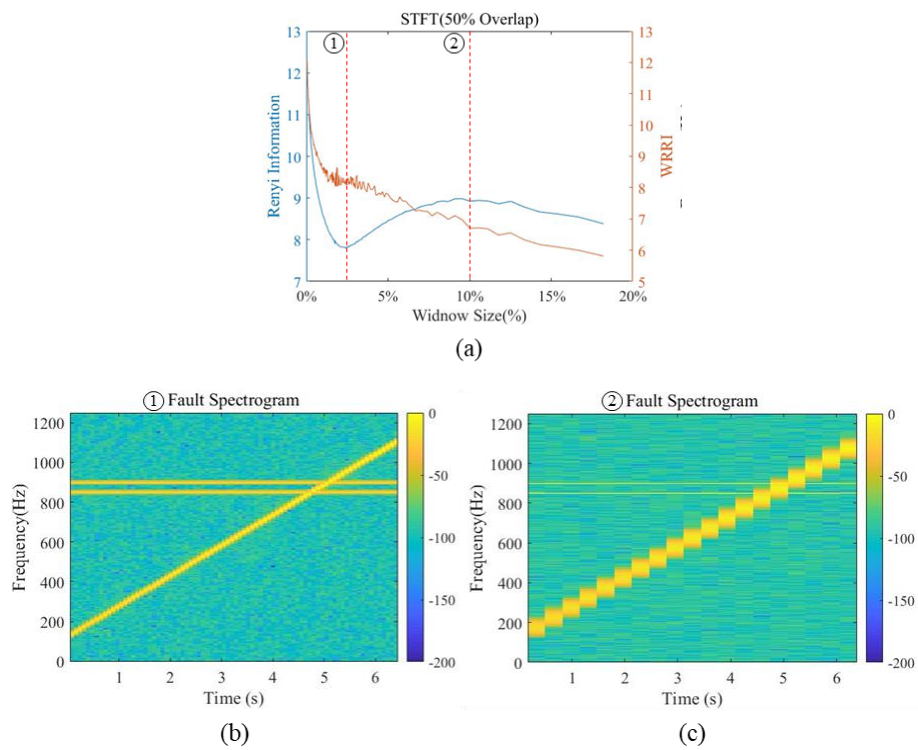

Figure 4-4. (a) Index plot for WRRI and Rényi Information, (b) Spectrogram at 2.4% window size of total signal length, and (c) Spectrogram at 10% window size of total window length

Index plot of non-stationary signal with impulse type of fault feature has different minimum points for WRRI and Rényi Information as shown in Figure 4-2. The minimum point of Rényi Information determines that the spectrogram using a window size of 2.4% of the total signal length is the sharpest representation. However, the minimum point of WRRI is judged that the spectrogram using the window size of 1.4% of the total signal length is the sharpest representation. As confirmed in Chapter 3.1, the spectrogram suggested by WRRI to have a 1.4% window size is more advantageous in detecting the impulse type of fault feature. Since it is WRRI that adds emphasis to the impulse type of fault feature that appears with the ridge signal, it is a better measure for the detecting fault feature.

For the Mixture of two fault features, the WRRI and Rényi Information index plots show the same trend. The difference is that fluctuation appears in the proposed measure, WRRI. This fluctuation is the cause of the fault feature, which can be confirmed through the Rényi Information results in Figure 3-3. Also, in the case of Rényi Information, since there is no discrimination between fault feature and ridge signal, the influence is not shown in the index plot of the entire signal.

Considering the case where the characteristic frequency is added linearly with the ridge signal, the fault feature is a frequency component, so the TFR measure should propose a parameter toward improving the frequency resolution. Reflecting that, the WRRI Index plot shows a consistent trend. However, Rényi Information does not consistently express that trend. It shows the local minimum point and tends to increase and then decrease again. In the case of Rényi Information, which does not show the proper trend according to the fault feature, it means that it is not possible to choose an appropriate parameter in analyzing the actual fault state signal. Therefore, we can see that WRRI is a better TFR measure for detecting fault features in these cases.

4.2 Experiment Signal

In the validation process using the experiment signal, two types of rotating machinery are considered; motor and planetary gearbox. Also, to consider the effects on the speed profile, each machinery was operated at two speed profiles. The first experiment signals were acquired from the planetary gearbox. The description and detail of the gearbox test-bed are illustrated in Park et al [7] article. Health state signal and fault state signal were obtained from the testbed and the target failure mode is the tooth crack of the planet gear. The raw vibration signal for each speed profile is in Figure 4-5.

The difference between the health state signal and fault state signals was not very discernable. As such, if the fault features are little discerned, it could be expected that the existing Rényi Information and the proposed WRRI will not show much difference, and the results are shown in Figure 4-6.

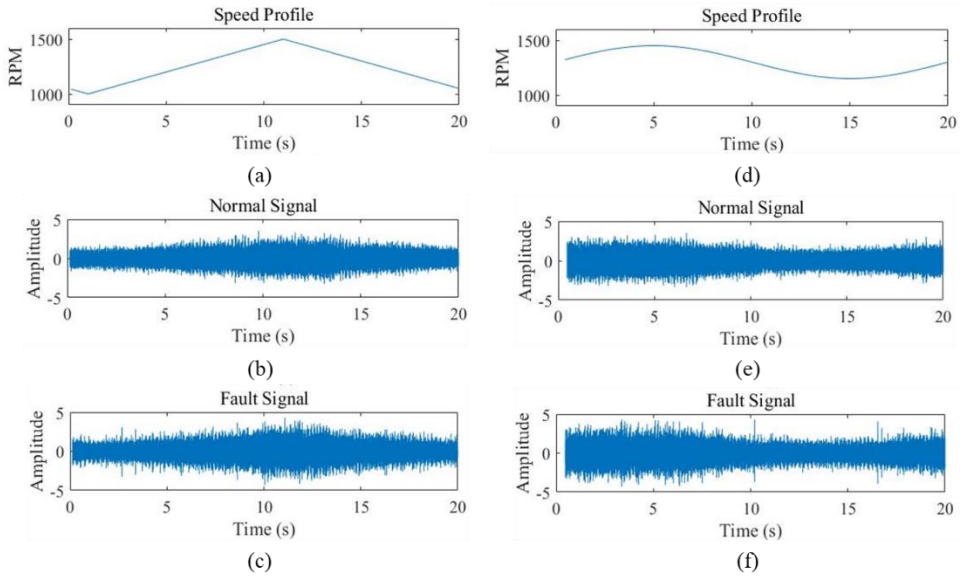

Figure 4-5. Triangular speed profile of (a) RPM, (b) health state signal, (c) fault state signal of the gearbox. Sinusoidal speed profile of (d) RPM, (e) health state signal, (f) fault state signal of the gearbox.

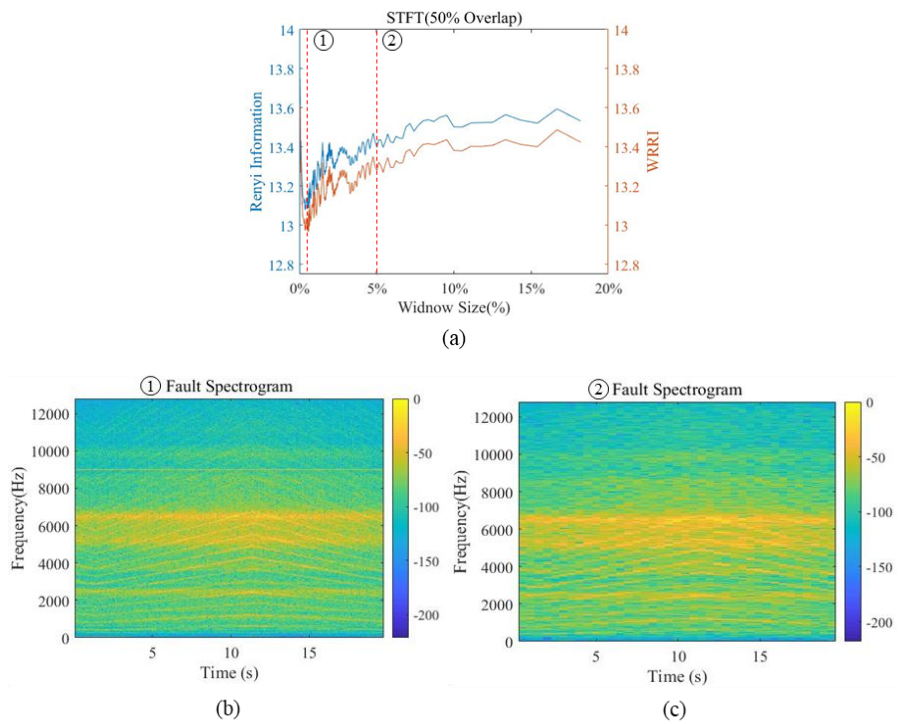

Figure 4-6. Triangular speed profile (a) measure value of the gearbox according to window size, (b) spectrogram at 0.56% window size, (c) spectrogram at 5% window size.

It shows the same tendency as both measures and says that it is the optimal representation for the 0.56% window size. For comparison, plotting the representation at a 5% window size shows that 0.56% is a better representation from a readability perspective. In order to check whether the same tendency is made from the viewpoint of detectability, the fault feature of the spectrogram made of 0.56% and 5% window size is calculated using the Frobenius norm.

$$\|A\|_F := \left(\sum_{i=1}^{m} \sum_{j=1}^{n} |P_{ij}|^2 \right)^{1/2} \tag{4-2}$$

The Frobenius norm is well used to quantify the matrix in machine learning and deep learning area [37]–[39]. Besides, quantification was conducted by subtracting from health state matrix and fault state matrix, or subtracting from matrix quantified values. In the same way, they were quantified using only the values around 5000~7000 Hz corresponding to the excitation band.

From all the values provided in the table, it can be seen that the quantification value of health and fault state is large at 0.56% window size. Therefore, in terms of detectability, the representation at 0.56% window size is better than the other. Additionally, the fluctuation of the index is mainly the result of the relationship between excitation band and frequency resolution. The unexpected characteristic frequency component excited near 9000 Hz also contributes to this trend.

For the case of sinusoidal speed profile, it shows same result with triangular speed profile. The trend of the two measures is the same and recommends the same window size from the point of readability and detectability.

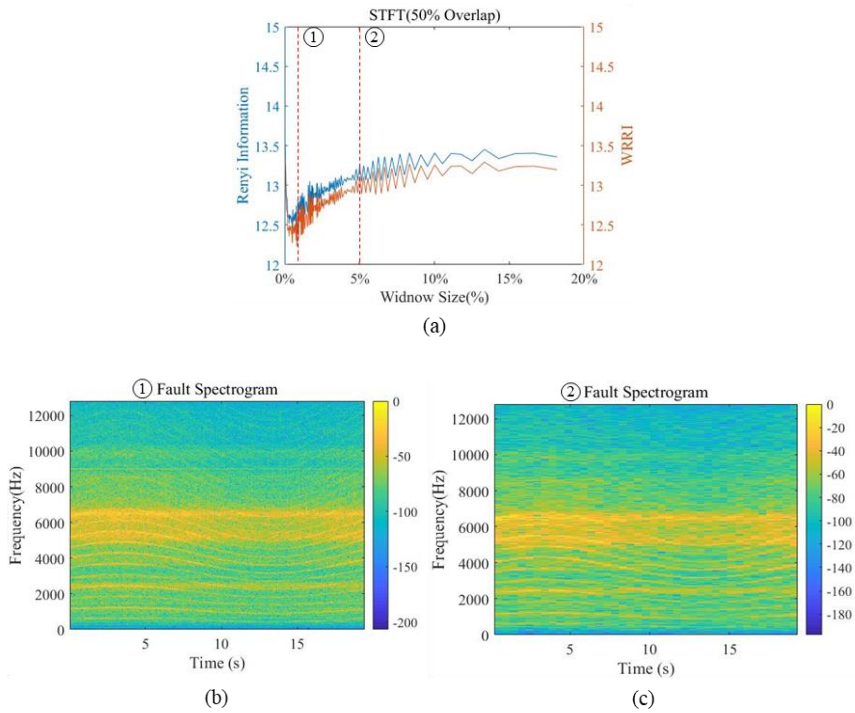

Figure 4-7. Sinusoidal speed profile (a) measure value of the gearbox according to window size, (b) spectrogram at 0.80% window size, (c) spectrogram at 5% window size.

Table 4-1. Quantification result of triangular speed profile spectrogram of the gearbox

	$\|\|A\|\|_{F_f-F_n}$	$\|\|A\|\|_{F_f} - \|\|A\|\|_{F_n}$	$\|\|A\|\|_{F_f-F_n,\ BPF}$	$\|\|A\|\|_{F_f,\ BPF} - \|\|A\|\|_{F_n,\ BPF}$
0.56% Window size	0.0112	0.0038	0.0107	0.0042
5% Window size	0.0087	0.0033	0.0083	0.0036

Table 4-2. Quantification result of sinusoidal speed profile spectrogram of the gearbox

	$\|\|A\|\|_{F_f-F_n}$	$\|\|A\|\|_{F_f} - \|\|A\|\|_{F_n}$	$\|\|A\|\|_{F_f-F_n,\ BPF}$	$\|\|A\|\|_{F_f,\ BPF} - \|\|A\|\|_{F_n,\ BPF}$
0.8% Window size	0.0093	0.00228	0.0088	0.0026
5% Window size	0.0082	0.00226	0.0078	0.0024

Because the fault feature is less distinguishable, there is no difference between the two measures in the index plot. This result is the same in WT as well as in STFT. As for the CWT, the value of the measure is as shown in Figure 4-8 while changing the decay parameter β and symmetry parameter γ of the Generalized Morse wavelet described in Chapter 2.1. Within the range observed while changing the parameters, both measures showed the same index plot.

It can be seen that this depends on the wavelet duration, $P_{\beta,\gamma}$, of the product of the two parameters. Although there was no difference between the measures within the parameter range covered in this study, it was shown that it can be used as a role to select parameters of CWT. Also, this role of measures was available in DWT. As a result of using MODWT for various types of wavelets, Rényi Information and WRRI showed only the difference in value level, and the trend itself was the same.

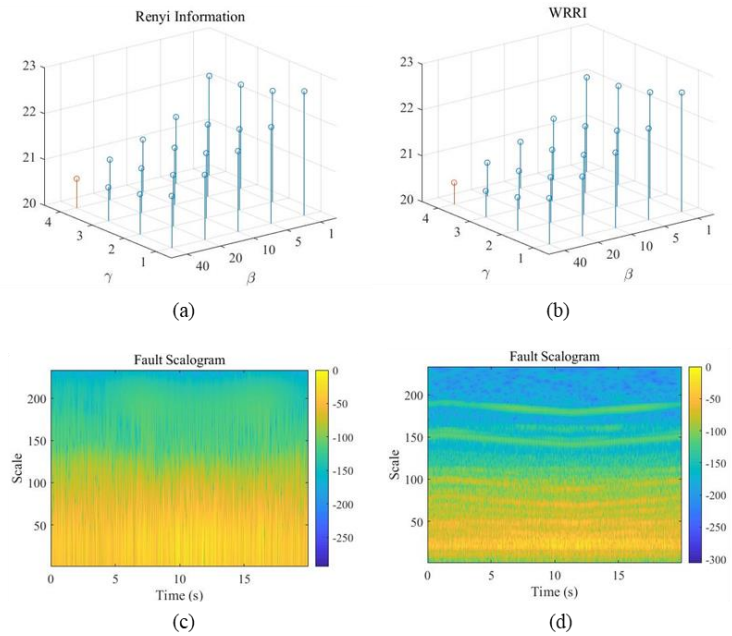

Figure 4-8. Triangular speed profile measure value of the gearbox according to β and γ (a) Rényi Information, (b) WRRI, (c) Scalogram at $\beta = 1$, $\gamma = 1$, (d) Scalogram at $\beta = 40$, $\gamma = 4$.

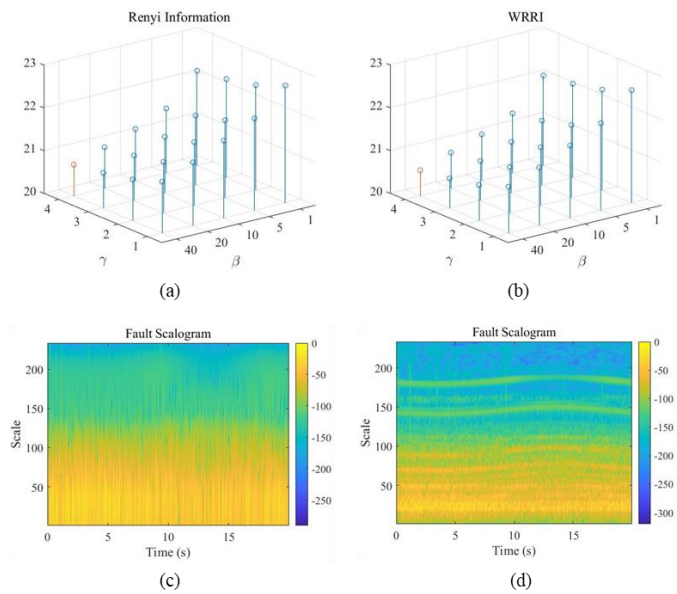

Figure 4-9. Sinusoidal speed profile measure value of the gearbox according to β and γ (a) Rényi Information, (b) WRRI, (c) Scalogram at $\beta = 1$, $\gamma = 1$, (d) Scalogram at $\beta = 40$, $\gamma = 4$

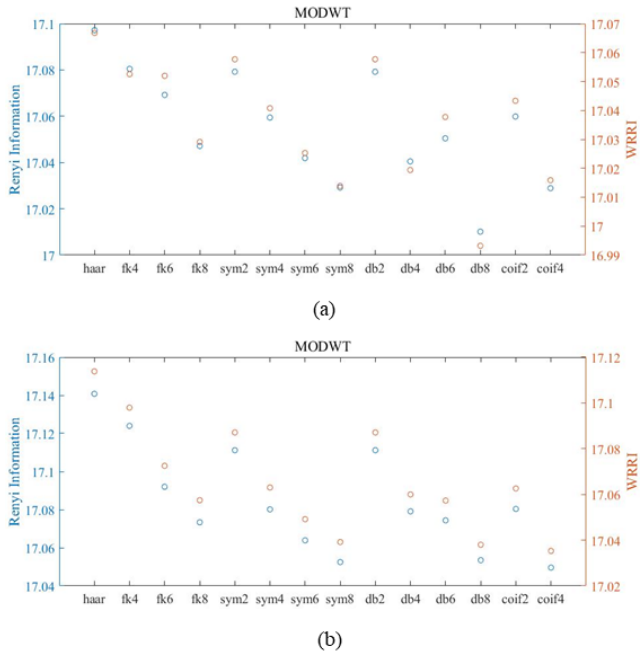

Figure 4-10. Measure value of the gearbox using MODWT (a) Triangular speed profile, (b) Sinusoidal speed profile.

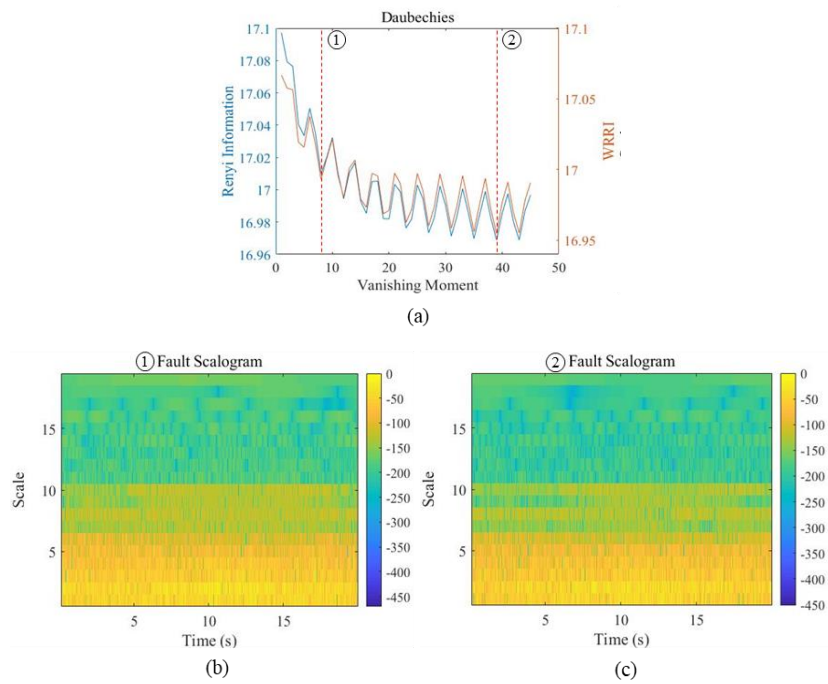

Figure 4-11. Triangular speed profile (a) Index plot for WRRI and Rényi Information depend on the vanishing moment, (b) Scalogram using db8, (c) Spectrogram using db39

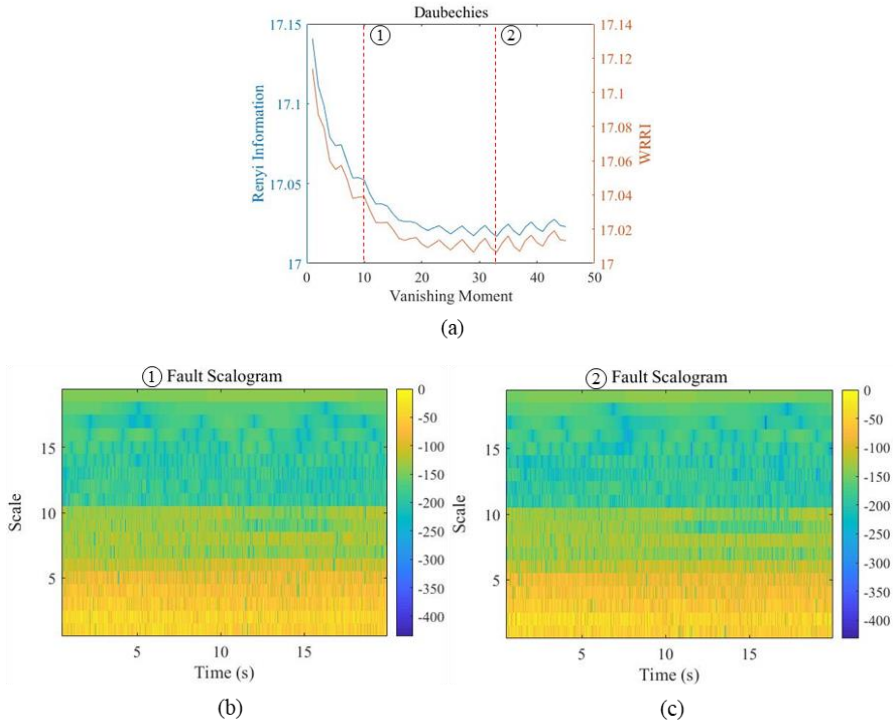

Figure 4-12. Sinusoidal speed profile (a) Index plot for WRRI and Rényi Information depend on the vanishing moment, (b) Scalogram using db10, (c) Spectrogram using db34

Table 4-3. Quantification result of Scalogram of the gearbox depend on vanishing moment

	Triangular speed profile		Sinusoidal speed profile	
	db8	db39	db10	db33
$\|\|A\|\|_{F_f - F_n}$	0.0027	0.0028	0.0026	0.0027
$\|\|A\|\|_{F_f} - \|\|A\|\|_{F_n}$	6.325e-4	5.887e-4	4.602e-4	4.241e-4

The Daubechies wavelet, which is considered a good wavelet for both speed profiles, was calculated by adjusting the vanishing moment. The results are as shown in Figure 4-11, Figure 4-12. When we used the MODWT, it is difficult to observe the speed change in the shifting conditions. In this case, it can be seen that it is not meant to select a good wavelet in the aspect of readability using Rényi Information. Even if it shows the same trend, in terms of detectability, it still produces valid results because the target is in the fault feature.

The minimum value can be obtained by examining the measure value by changing the vanishing moment, but the width of the value is not large. The difference in TFR that is selected based on a difference value of about 0.15 does not make a big difference even in actual quantification.

Summarizing the results of STFT and CWT for the two speed profiles of the gearbox, Rényi Information and WRRI do not show a difference for signals where the fault feature is not clearly noticeable. However, both Rényi Information and WRRI were able to select TFR parameters in terms of readability and detectability, respectively. And the process was confirmed by spectrogram, scalogram, and quantification using Frobenius norm. Therefore, the proposed WRRI can play the role of Rényi Information even when the fault feature is not prominent. For cases where fault features are discerned, we present a motor test case to see if WRRI can actually suggest a better TFR.

The second validation process is performed based on the signals acquired through the motor testbed. The testbed uses permanent magnet synchronous motor (PMSM) seeding stator inter-turn short circuit fault.

The overall configuration of the testbed is shown in Figure 4-13. The Welcon System's servo driver was used to drive the motor. And hysteresis brake which used for the role of the external load was Magtrol’s product. There are data obtained from the torque sensor and the acceleration sensor, but in this study, only one of the three-phase current measured with the current probe Tektroniks A622 was used. And the target motor used is a 10-pole pair, 200W motor from TMTECH-I Co.

The speed profile acquired from the torque sensor and raw current signal form the current prove for the validation are as follows.

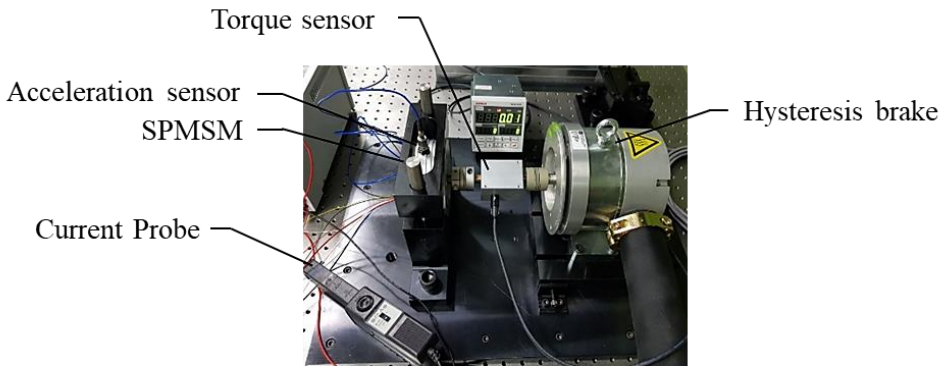

Figure 4-13. Overall configuration of the PMSM testbed

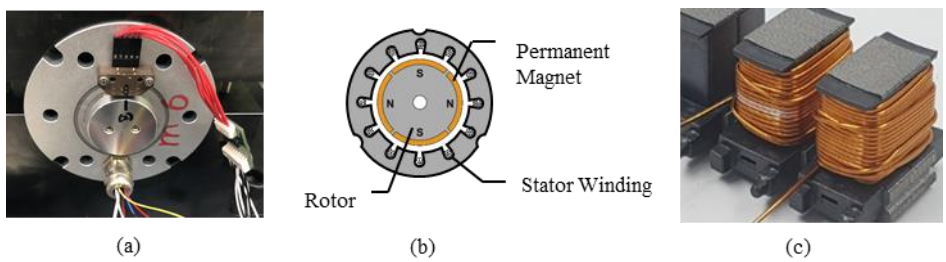

Figure 4-14. (a) Testbed target motor, (b) schematic cross-sectional view of PMSM, (c) inter-turn short in the PMSM

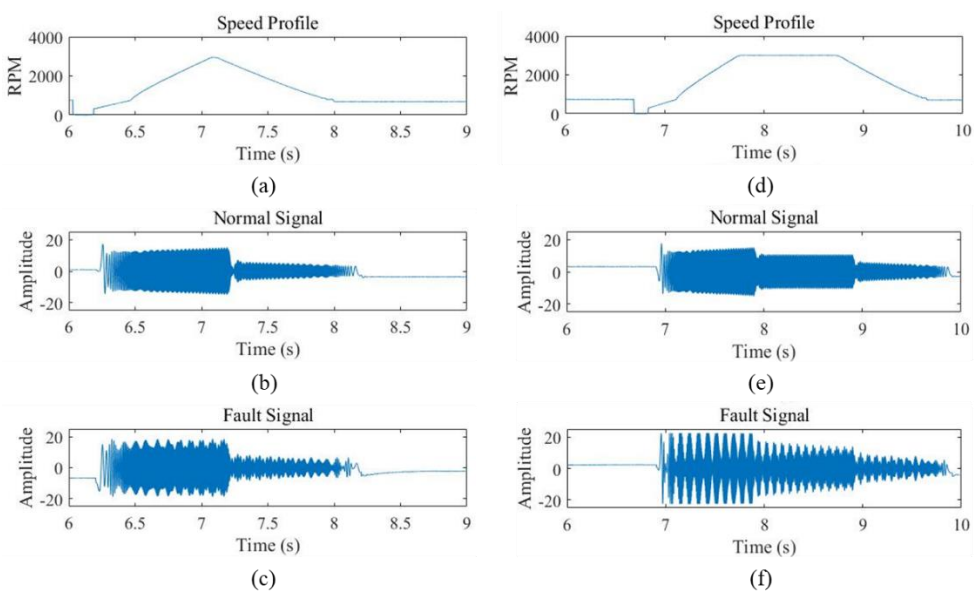

Figure 4-15. Triangular speed profile of (a) RPM, (b) health state signal, (c) fault state signal. Trapezoidal speed profile of (d) RPM, (e) health state signal, (f) fault state signal.

Unlike the planetary gearbox vibration signal, the fault feature is clearly discernable in the PMSM current signal so that it can be visually confirmed. For these signals, we compared the measure values according to the window size for using the spectrogram. According to the characteristics of the information-based measure, which means that the smaller the value, the better the expression, Rényi information and WRRI show different minimum points. As shown in Figure 4-16, spectrograms were drawn for the window size where each measure points to the minimum value.

However, in the figure, human eyes make it confused to choose (a) is the better representation to show the signals.

It is intuitively clear from a readability point of view that the TFR created by Rényi information looks clearer than the TFR produced by WRRI. However, considering the fault feature as a reference, it is possible to explain why WRRI chose the figure (c). First, in the inter-turn short circuit of PMSM, the three-phase balance is broken due to the short-phase, and the triplex component of the PWM supply frequency appears due to this imbalance. This phenomenon appears mainly as a frequency component at three times the supply frequency [40], [41]. Therefore, it is not surprising that WRRI created a spectrogram that improved the frequency resolution by selecting a wide window size to emphasize this characteristic frequency. Also, an example resolution box for window size is shown in Figure 4-17. Because the large window size seems to blur horizontally, the result shown in Figure 4-16 looks less intuitive.

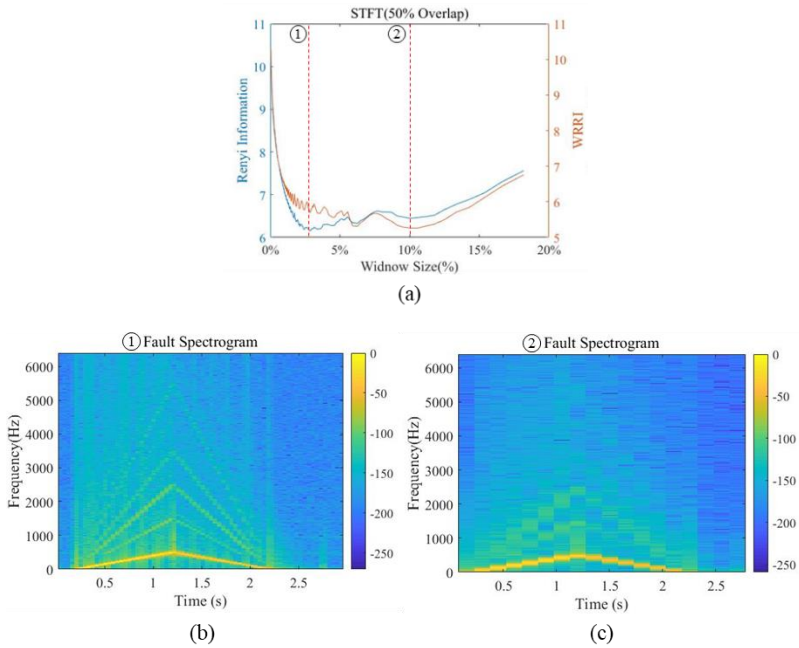

Figure 4-16. Triangular speed profile (a) Measure value comparison according to window size, (b) spectrogram at Rényi information measure minimum point, (c) spectrogram at WRRI measure minimum point

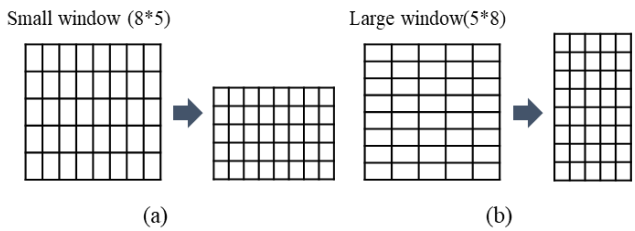

Figure 4-17. Resolution box example

Table 4-4. Quantification result of triangular speed profile spectrogram of the motor

	$\|A\|_{F_f-F_n}$	$\|A\|_{F_f} - \|A\|_{F_n}$	$\|A\|_{F_f-F_n,\ LPF}$	$\|A\|_{F_f,\ LPF} - \|A\|_{F_n,\ LPF}$	$\|A\|_{F_f-F_n,\ HPF}$	$\|A\|_{F_f,\ HPF} - \|A\|_{F_n,\ HPF}$
2.8% Window size	0.0808	0.0445	0.0808	0.0445	1.0222e-5	8.0162e-6
10% Window size	0.0961	0.0495	0.0964	0.0495	1.1557e-5	8.2639e-6

Quantification was conducted by subtracting from health and fault state matrix or subtracting from matrix quantified values. In the same way, they were quantified using only the values above rotating frequency or under characteristic frequency. In the current signal, the rotating supply frequency appears along with the speed profile. For a motor speed profile with a peak of 3000 RPM, 500 Hz appears as the peak rotating frequency. Therefore, the quantification of only the values after the 500 Hz range was called HPF, and the case of using only values below 1500 Hz, which is the 3rd order harmonic frequency, was called LPF. From the quantification results, it can be seen that the value is higher in the TFR proposed by WRRI. The implication of this result is that the representation made by window size suggested by WRRI makes the difference between health and fault state bigger. In order to check the effect of the above results on the actual diagnosis, the diagnosis results were confirmed through a deep learning model capable of autonomous feature extraction rather than an arbitrary user. The convolutional neural network (CNN) based deep learning model used for diagnosis is VGGNet, which shows greater utility and scalability than the actual winning algorithm with a simple structure, and is the model that won the 2nd prize in ImageNet Large Scale Visual Recognition Challenge (ILSVRC) at 2014 [42]. Since the TFR is different for each window size and the matrix size at this time is different, the input structure of the model is designed differently accordingly, but the number of channels and the structure of the layers is designed in the same way as VGGNet.

Spectrograms were made with a total of 90 identical speed profiles, of which 60% were used for training and 40% were used for validation. Also, considering that the model was trained with little data, the model was repeatedly trained 10 times and the result was shown using a boxplot. No further work has been done because what we want to check with this diagnostic model is training ability and accuracy. Training loss was reduced as a result of training with the model, and the trend was not different for both spectrograms. However, in terms of generalization

performance, the accuracy converged to 100% when trained with the spectrogram selected by WRRI, and the accuracy converged near 88% when trained with the spectrogram selected by Rényi Information.

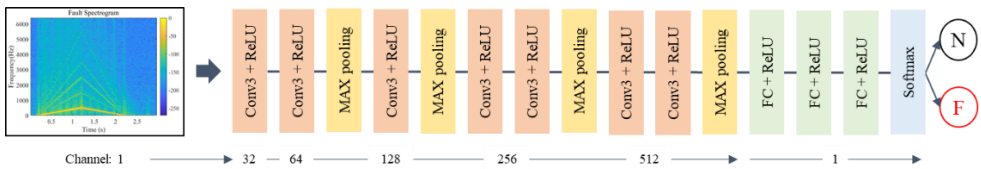

Figure 4-18. VGGNet based CNN model for fault diagnosis with spectrogram as input

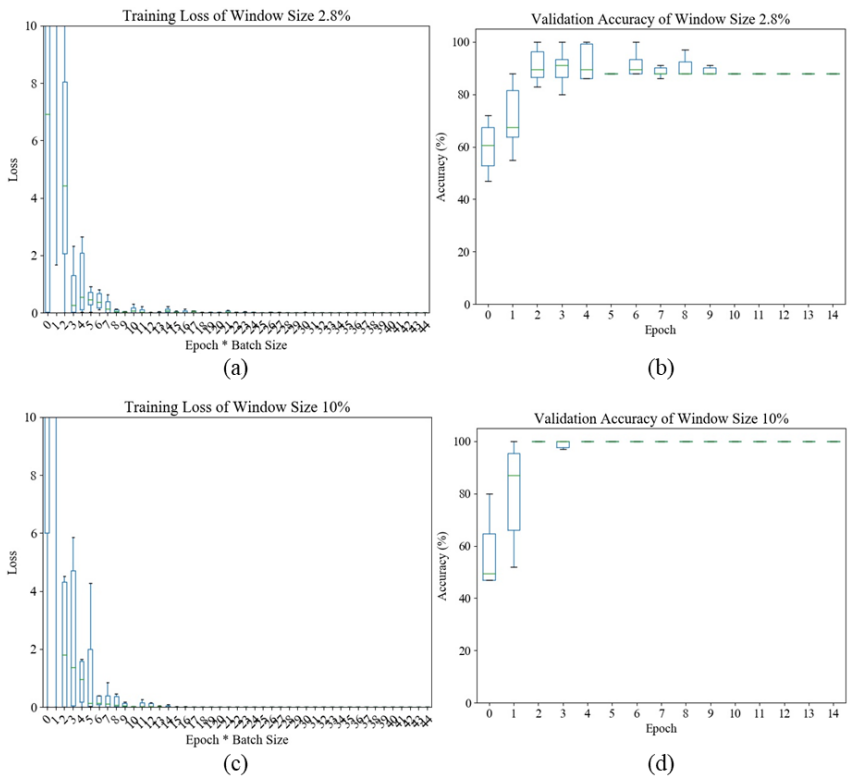

Figure 4-19. Result of (a) Training loss, (b) Validation accuracy using 2.8% window size spectrogram, (c) Training loss, and (d) Validation accuracy using 10% window size spectrogram as an input

Both the quantification result and the diagnostic result prove that the window size proposed by WRRI better expresses the fault feature. Additionally, in the case of the trapezoidal speed profile, two measures show a different trend. Even in the case of Rényi Information tend to make the representation having a bigger and bigger window. WRRI shows a local minimum point around 1.3% window size, but it also shows the tendency that the value decreases gradually.

Although the trend of Rényi Information is interpreted from the viewpoint of readability, it can be seen that it is not suitable for analyzing signals under variable speed conditions. Compared with the triangular speed profile, the suggestion of larger window size is due to the longer length of the constant velocity section. In other words, Rényi Information suggests that this non-stationary signal is a quasi-stationary signal and performs a simple Fourier transform. These results are undesirable for time-frequency analysis in variable speed conditions. However, through the fact that this trend also appears in WRRI, it was confirmed that the larger the window size, the more the effect on the constant velocity section was reflected. Therefore, we have confirmed that for WRRI and Rényi Information, when the length of the constant speed section is long and the variable speed is short, measures lead to an analysis by a simple Fourier transform. And this tendency is relatively less significant because WRRI focuses on the fault feature.

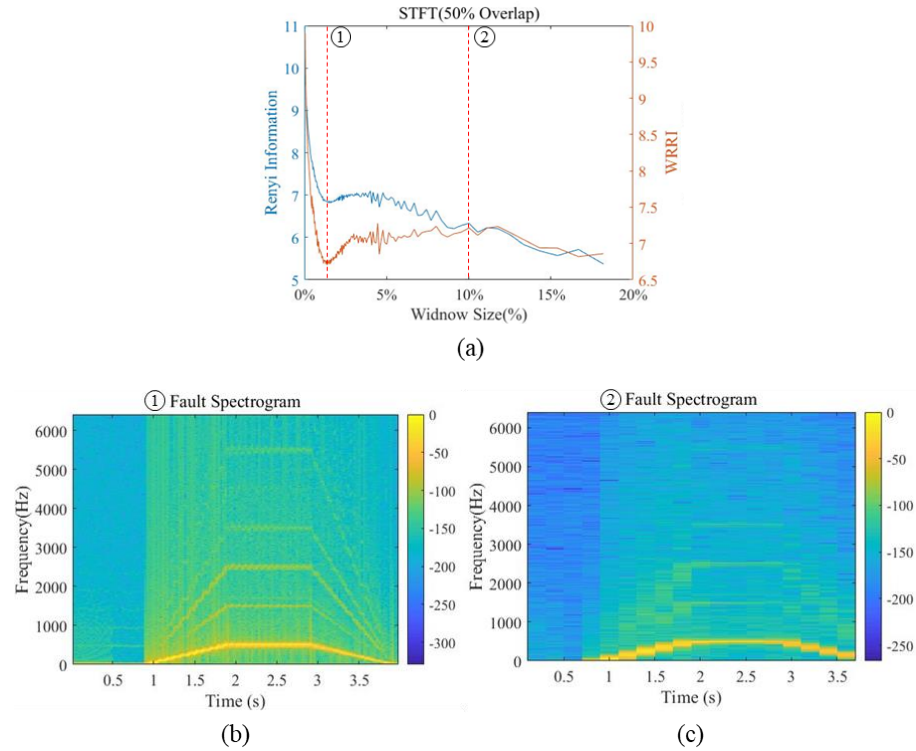

Figure 4-20. Trapezoidal (a) Measure value comparison according to window size, (b) spectrogram at WRRI measure minimum point, (c) spectrogram at the 10% window size

Table 4-5. Quantification result of trapezoidal speed profile spectrogram of the motor

	$\|A\|_{F_f-F_n}$	$\|A\|_{F_f} - \|A\|_{F_n}$	$\|A\|_{F_f-F_n,\ LPF}$	$\|A\|_{F_f,\ LPF} - \|A\|_{F_n,\ LPF}$	$\|A\|_{F_f-F_n,\ HPF}$	$\|A\|_{F_f,\ HPF} - \|A\|_{F_n,\ HPF}$
1.36.% Window size	0.0695	0.0423	4.906e-5	4.346e-5	0.0695	0.0423
10% Window size	0.0436	0.0154	4.819e-5	4.201e-5	0.0436	0.0154

The quantification result was a comparison of the local minimum of WRRI and the value at 10% window size, and it was confirmed that the difference was large at the local minimum of WRRI. Also, the same with the triangular speed profile, VGGNet based fault diagnosis model is used to automatically extract fault feature and diagnosis fault.

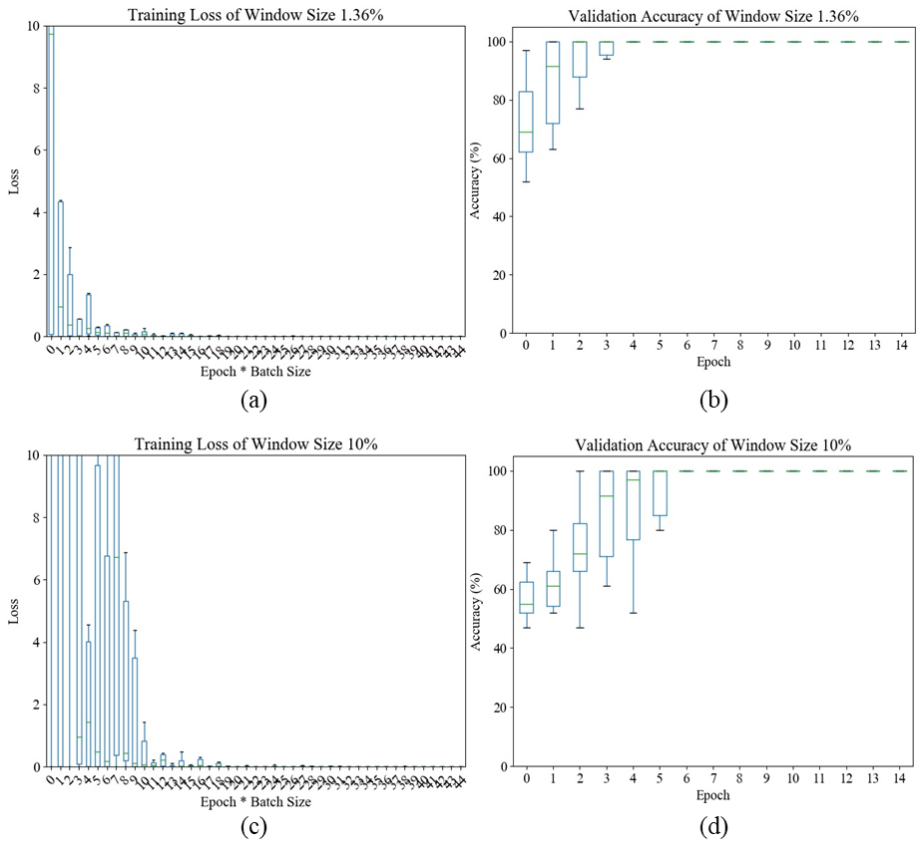

Figure 4-21. Result of (a) Training loss, (b) Validation accuracy using 1.36% window size spectrogram, (c) Training loss, and (d) Validation accuracy using 10% window size spectrogram as an input

Compared to the triangular speed profile diagnosis result, it was confirmed that the validation accuracy increased to 100% even at a 10% window size. However, it can be seen that when the window size is 1.36%, the training loss decrease and accuracy increase faster than the 10% window size. This means that there is a lot of information available in model training to classify health and fault state. This result, together with the quantification result, explains that WRRI better expresses the fault feature.

In the case of using CWT, the value of the measure is as shown in Figure 4-22 while changing the decay parameter β and symmetry parameter γ of the Generalized Morse wavelet described in Chapter 2.1. Within the range observed while changing the parameters, both measures showed the same index plot.

The difference according to the parameter change of the Generalized Morse wavelet was confirmed, but the difference between the two measures was not discernible. This is presumed to be because the influence of the wavelet parameter is greater than the weight on the fault feature. This trend is the same in the trapezoidal speed profile case in Figure 4-23.

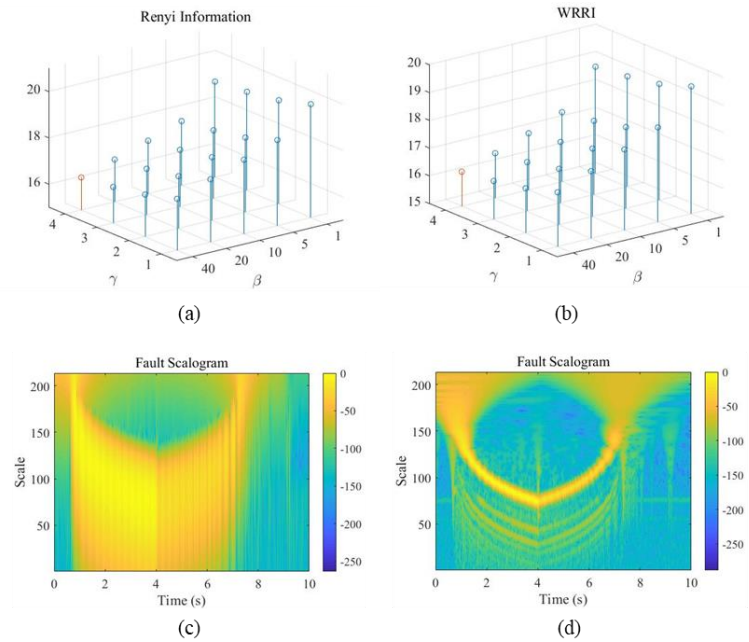

Figure 4-22. Triangular speed profile measure value of the motor according to β and γ (a) Rényi Information, (b) WRRI, (c) Scalogram at $\beta = 1$, $\gamma = 1$, (d) Scalogram at $\beta = 40, \quad \gamma = 4$

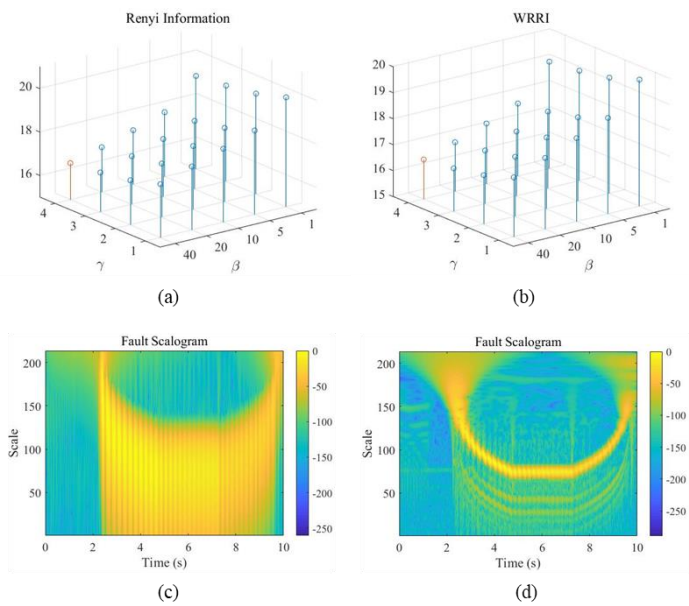

Figure 4-23. Trapezoidal speed profile measure value of the motor according to β and γ (a) Rényi Information, (b) WRRI, (c) Scalogram at $\beta = 1$, $\gamma = 1$, (d) Scalogram at $\beta = 40, \quad \gamma = 4$

Also, in the case of DWT, there is no difference in the rank of the values that the two measures represent for each wavelet, and the difference between the values is not significant. Besides, the results of each vanishing moment for the Daubechies wavelet are shown in the figure below. WRRI and Rényi Information show the same tendency for triangular and trapezoidal speed profiles, although the level of the value is different.

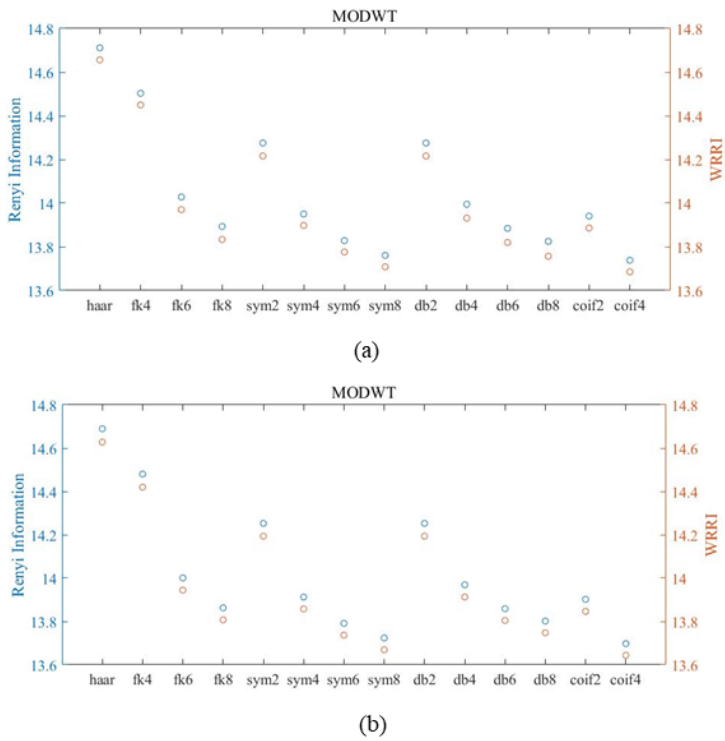

Figure 4-24. Measure value of the motor using MODWT (a) Triangular speed profile, (b) Trapezoidal speed profile

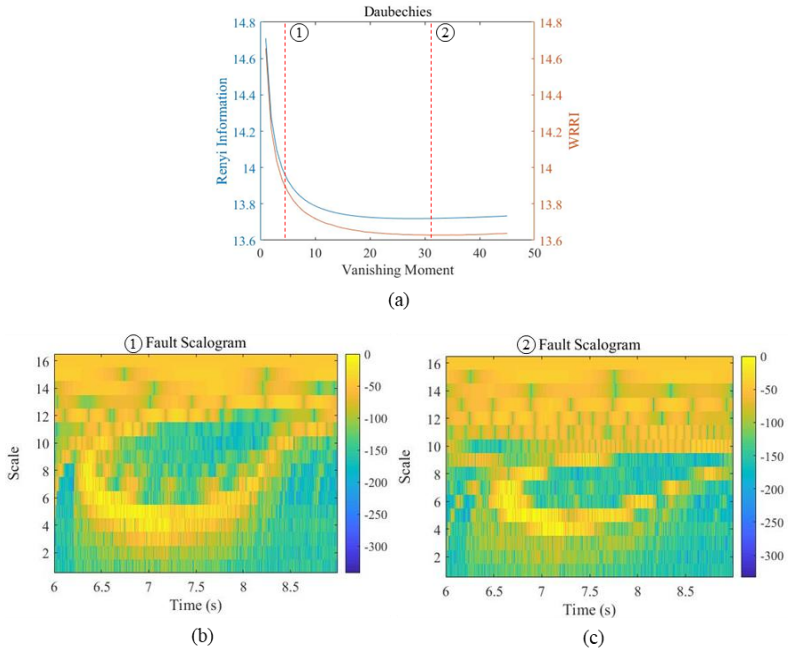

Figure 4-25. Triangular speed profile of the motor (a) Index plot for WRRI and Rényi Information depend on the vanishing moment, (b) Scalogram using db4, (c) Spectrogram using db31

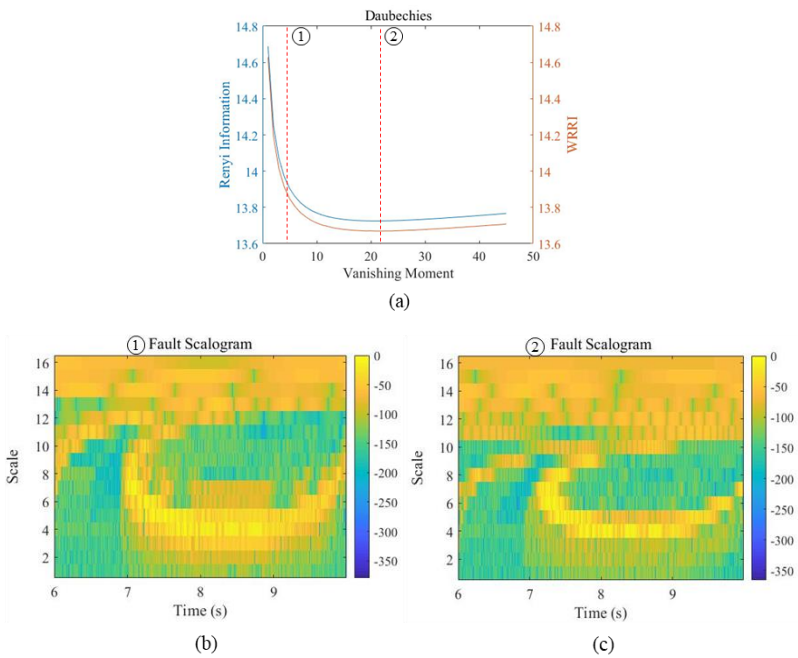

Figure 4-26. Trapezoidal speed profile of the motor (a) Index plot for WRRI and Rényi Information depend on the vanishing moment, (b) Scalogram using db4, (c) Spectrogram using db22

The graph shape of the index plot according to the vanishing moment decreases to a certain value level and then tends to converge to a specific value. By using this graph, it is possible to select a better representation through the wavelet, which can be confirmed in the Scalogram. In the graph above, the minimum value selected by each measure was db31 for WRRI, db28 for Rényi Information in the triangular speed profile, db22 for WRRI, and db21 for Rényi Information in the trapezoidal speed profile. However, since the difference in the value of the measure is very small, it is difficult to say that it shows a difference.

When considering this result with the gearbox case, it can be seen that WT produces a small measure value difference according to the wavelets in contrast to the result that differs depending on the difference in window size in STFT. Also, the level of measure value varies depending on the type of wavelet, and the emphasis on fault feature is not revealed in the measure value. Differences between inner product formulation and multi-resolution with the wavelet serve as a candidate to reduce the difference in measure values compared to the STFT case.

Summarizing the validation results for the two types of rotating machineries, the difference between the health and the fault state was not discerned significantly in the planetary gearbox, as can be seen from the raw signal. This was reflected in the calculation of two measures, and confirmed that it did not make a difference between existing Rényi Information and WRRI through STFT, CWT, and DWT. However, through these results, we showed that WRRI showed the same directionality as that of Rényi Information, and acted as Rényi information when the fault feature was small. In the motor testbed, the fault feature existed enough to be discerned visually. In this case, Rényi Information and WRRI showed different trends, and in the case of STFT, the difference was marked. The quantification result and deep learning diagnostic model proved that WRRI is more useful for fault diagnosis and feature extraction. However, in the case of CWT and DWT, WRRI showed almost the same shape as Rényi Information, and the difference was slight.

When interpreting the motor verification contents together with the results of CWT and DWT in the gearbox, WT does not have a large change in the measure value according to the parameter change. Also, the variation in measure value due to parameter change was larger than the variation in measure value caused by emphasizing the fault feature of the experimental signal.

Chapter 5. Conclusion

In this study, a TFR measure for fault diagnosis is proposed. By comparing the TFR measures proposed in the previous signal processing studies through a simple comparative study, it was confirmed that Rényi Information has good performance. Since the measure to be proposed was aimed at fault diagnosis, a perspective of detectability for fault features was presented. Based on this, the proposed measure was designed to transform the *atom* of Rényi Information and consisted of residual term and weighting term in terms of detecting the fault feature.

The process of verifying the proposed measure was performed through an analytic signal and a rotating machinery signal. The analytic signal was performed on signals with a combination of linear chirp with three fault features; impulse type of fault feature, mixture type of fault feature, and characteristic frequency. Through this, it was verified that the use of the parameters suggested by WRRI better expresses the fault feature. Also, a verification process was performed on the planetary gearbox testbed, which does not reveal the fault feature, and the motor testbed, where the fault feature is well revealed. In the case of planetary gearbox, both WRRI and Rényi Information served as measures for better expression but showed the same tendency. Through this, WRRI showed that it is possible to perform the role of Rényi Information even when fault feature is not discerned. In the case of the motor testbed, the WRRI and Rényi Information showed a significant difference in the STFT, and for each of them, through the Frobenius norm and CNN based diagnosis model, it was verified that the expression proposed by WRRI is a better representation for fault diagnosis and feature extraction.

In the case of the signal used for validation in this study, it was difficult to clearly distinguish the difference in the wavelet transform. After that, through the verification process for various speed profiles and rotating machinery, we intend to secure expandability that can be used for various TFRs including WT.

Bibliography

[1] J. Lee, F. Wu, W. Zhao, M. Ghaffari, L. Liao, and D. Siegel, “Prognostics and health management design for rotary machinery systems - Reviews, methodology and applications,” *Mech. Syst. Signal Process.*, vol. 42, no. 1–2, pp. 314–334, 2014.

[2] B. Volponi, A., and Wood, “Engine health management for aircraft propulsion systems,” *Forum Integr. Syst. Heal. Eng. Manag. Aerosp.*, pp. 7–10, 2005.

[3] J. M. Ha, J. Park, K. Na, Y. Kim, and B. D. Youn, “Toothwise Fault Identification for a Planetary Gearbox Based on a Health Data Map,” *IEEE Trans. Ind. Electron.*, vol. 65, no. 7, pp. 5903–5912, 2018.

[4] T. Praveenkumar, M. Saimurugan, and K. I. Ramachandran, “Comparison of vibration, sound and motor current signature analysis for detection of gear box faults,” *Int. J. Progn. Heal. Manag.*, vol. 8, no. 2, 2017.

[5] Z. Feng, M. Liang, and F. Chu, “Recent advances in time-frequency analysis methods for machinery fault diagnosis: A review with application examples,” *Mechanical Systems and Signal Processing*, vol. 38, no. 1. pp. 165–205, 2013.

[6] H. Hong and M. Liang, “Separation of fault features from a single-channel mechanical signal mixture using wavelet decomposition,” *Mech. Syst. Signal Process.*, vol. 21, no. 5, pp. 2025–2040, 2007.

[7] J. Park, M. Hamadache, J. M. Ha, Y. Kim, K. Na, and B. D. Youn, “A positive energy residual (PER) based planetary gear fault detection method under variable speed conditions,” *Mech. Syst. Signal Process.*, vol. 117, pp.

347–360, Feb. 2019.

[8] P. W. Tse, F. L. Chu, and Z. K. Peng, “A comparison study of improved Hilbert–Huang transform and wavelet transform: Application to fault diagnosis for rolling bearing,” *Mechanical Systems and Signal Processing*, vol. 19, no. 5. pp. 974–988, 2005.

[9] C. Li and M. Liang, “Timefrequency signal analysis for gearbox fault diagnosis using a generalized synchrosqueezing transform,” *Mech. Syst. Signal Process.*, vol. 26, no. 1, pp. 205–217, 2012.

[10] DAUBECHIES and I., “A Nonlinear Squeezing of the Continuous Wavelet Transform Based on Auditory Nerve Models,” *Wavelets Med. Biol.*, pp. 527–546, 1996.

[11] Z. Feng, X. Chen, and T. Wang, “Time-varying demodulation analysis for rolling bearing fault diagnosis under variable speed conditions,” *J. Sound Vib.*, vol. 400, pp. 71–85, 2017.

[12] I. Daubechies, Y. (Grace) Wang, and H. Wu, “ConceFT: concentration of frequency and time via a multitapered synchrosqueezed transform,” *Philos. Trans. R. Soc. A Math. Phys. Eng. Sci.*, vol. 374, no. 2065, p. 20150193, Apr. 2016.

[13] Z. Feng and M. Liang, “Fault diagnosis of wind turbine planetary gearbox under nonstationary conditions via adaptive optimal kernel time-frequency analysis,” *Renew. Energy*, vol. 66, pp. 468–477, Jan. 2014.

[14] D. L. Jones and R. G. Baraniuk, “An Adaptive Optimal-Kernel Time-Frequency Representation,” *IEEE Trans. Signal Process.*, vol. 43, no. 10, pp. 2361–2371, 1995.

[15] D. L. Jones and T. W. Parks, “A High Resolution Data-Adaptive Time-Frequency,” *IEEE Trans. Acoust.*, vol. 38, no. 12, 1990.

[16] L. Stankovi, “Measure of some time-frequency distributions concentration,” *Signal Processing*, vol. 81, no. 3, pp. 621–631, 2001.

[17] A. Rényi, “On measures of entropy and information,” *Proc. Fourth Berkeley Symp. Math. Stat. Probab.*, vol. 1, 1961.

[18] P. Flandrin, R. G. Baraniuk, and O. Michel, “Time-frequency complexity and information,” *ICASSP, IEEE Int. Conf. Acoust. Speech Signal Process. - Proc.*, vol. 3, no. 2, pp. III329–III332, 1994.

[19] S. Aviyente and W. J. Williams, “Minimum entropy time-frequency distributions,” *IEEE Signal Process. Lett.*, vol. 12, no. 1, pp. 37–40, 2005.

[20] W. J. Williams and J. Jeong, “Kernel Design for Reduced Interference Distributions,” *IEEE Trans. Signal Process.*, vol. 40, no. 2, pp. 402–412, 1992.

[21] W. J. Williams and T. Sang, “Adaptive RID kernels which minimize time-frequency uncertainty,” in *Proceedings of IEEE-SP International Symposium on Time-Frequency and Time-Scale Analysis*, 1994, pp. 96–99.

[22] F. Hlawatsch and G. F. Boudreaux-Bartels, “Linear and quadratic time-frequency signal representations,” *IEEE Signal Process. Mag.*, vol. 9, no. 2, pp. 21–67, 1992.

[23] P. Flandrin, *Time-frequency/time-scale analysis*. Academic Press, 1998.

[24] A. T. Percival, D. B., & Walden, *Wavelet Methods for Time Series Analysis*, vol. 4. Cambridge university press, 2000.

[25] G. P. Nason and R. von Sachs, “Wavelets in time-series analysis,” *Philos.*

Trans. R. Soc. London. Ser. A Math. Phys. Eng. Sci., vol. 357, no. 1760, pp. 2511–2526, Sep. 1999.

[26] L. Zhu, Y. Wang, and Q. Fan, "MODWT-ARMA model for time series prediction," *Appl. Math. Model.*, vol. 38, no. 5–6, pp. 1859–1865, Mar. 2014.

[27] I. Daubechies and T. Paul, "Time-frequency localisation operators-a geometric phase space approach: II. The use of dilations," *Inverse Probl.*, vol. 4, no. 3, p. 661, 1988.

[28] J. M. Lilly and S. C. Olhede, "Higher-order properties of analytic wavelets," *IEEE Trans. Signal Process.*, vol. 57, no. 1, pp. 146–160, 2009.

[29] J. M. Lilly and S. C. Olhede, "Generalized morse wavelets as a superfamily of analytic wavelets," *IEEE Trans. Signal Process.*, vol. 60, no. 11, pp. 6036–6041, 2012.

[30] F. Hlawatsch and F. Auger, *Time-Frequency Analysis: Concepts and Methods*. ISTE Limited, 2008.

[31] W. J. Williams, M. L. Brown, and A. O. Hero III, "Uncertainty, information, and time-frequency distributions," *Adv. Signal Process. Algorithms, Archit. Implementations II*, vol. 1566, no. 313, pp. 144–156, 1991.

[32] T. H. Sang and W. J. Williams, "Renyi information and signal-dependent optimal kernel design," in *ICASSP, IEEE International Conference on Acoustics, Speech and Signal Processing - Proceedings*, 1995, vol. 2, pp. 997–1000.

[33] W. J. Williams, "Reduced Interference Distributions: Biological

Applications and Interpretations," *Proc. IEEE*, vol. 84, no. 9, pp. 1264–1280, 1996.

[34] R. G. Baraniuk, P. Flandrin, A. J. E. M. Janssen, and O. J. J. Michel, "Measuring time-frequency information content using the Reényi entropies," *IEEE Trans. Inf. Theory*, vol. 47, no. 4, pp. 1391–1409, 2001.

[35] J. K. Hammond, *Fundamentals of Signal Processing*. 1999.

[36] Y. T. Sheen, "A complex filter for vibration signal demodulation in bearing defect diagnosis," *J. Sound Vib.*, vol. 276, no. 1–2, pp. 105–119, Sep. 2004.

[37] W. Yang, X. Zhang, Y. Tian, W. Wang, J. H. Xue, and Q. Liao, "Deep Learning for Single Image Super-Resolution: A Brief Review," *IEEE Trans. Multimed.*, vol. 21, no. 12, pp. 3106–3121, 2019.

[38] G. Mesnil *et al.*, "Unsupervised and Transfer Learning Challenge: a Deep Learning approach," in *Proceedings of the 2011 International Conference on Unsupervised and Transfer Learning workshop-volume 27*, 2011, pp. 97–111.

[39] A. C. Ian Goodfellow, Yoshua Bengio, *Deep Learning*. MIT Press, 2016.

[40] B. Du, S. Wu, S. Han, and S. Cui, "Interturn Fault Diagnosis Strategy for Interior Permanent-Magnet Synchronous Motor of Electric Vehicles Based on Digital Signal Processor," *IEEE Trans. Ind. Electron.*, vol. 63, no. 3, pp. 1694–1706, 2016.

[41] S. M. A. Cruz and A. J. M. Cardoso, "Diagnosis of stator inter-turn short circuits in DTC induction motor drives," *IEEE Trans. Ind. Appl.*, vol. 40, no. 5, pp. 1349–1360, Sep. 2004.

[42] K. Simonyan and A. Zisserman, "Very deep convolutional networks for

large-scale image recognition," *arXiv Prepr. arXiv1409.1556*, 2014.

국문 초록

변속 조건에서 운전되는 회전기기 고장진단을 위해 시간-주파수 표현을 사용한 많은 연구들이 수행되어왔다. 하지만 대부분의 연구에서 시간-주파수 표현의 파라미터는 연구자들에 의해 경험적으로 선택되었다. 또한 이전에 제안된 시간-주파수 표현 측정방법도 고장 진단을 위한 최적의 파라미터를 제안해주지 못한다. 본 연구에서는 고장 특징 검출을 목적으로 시간-주파수 표현의 파라미터를 제안해주는 측정방법을 제안한다.

제안 측정방법 가중 잔차 레니 정보(WRRI)는 이전 연구들에서 제안된 측정밥법들에 대한 비교연구를 통해 선정된 레니 정보에 기반한다. WRRI는 레니 정보의 입력 형태를 2가지 성분으로 구성된 변형 형태를 통해 정의된다. 첫 번째 성분은 고장 특징 추출을 위한 잔차성분이고, 두 번째 성분은 노이즈의 영향성을 줄이기 위한 가중성분이다.

검증 과정은 산술적 신호와 모터, 기어 박스로 이루어진 신호를 통해 2 단계로 진행된다. 산술적 신호를 사용한 검증과정에서 WRRI는 기존 측정 방법인 레니 정보보다 고장 특징 검출에 더 적합한 시간-주파수 표현 파라미터를 제안했다. 또한 모터와 기어박스 테스트베드 신호를 사용한 검증과정에서 WRRI는 레니 정보보다 고장 특징 추출과 진단에 더 적합한 시간-주파수 파라미터를 제안했다.

주제어: 시간-주파수 표현

고장 특징

고장 진단

레니 정보

모터

기어박스

학 번: 2018-28190